Construction and Building Materials 438 (2024) 137154

Contents lists available at ScienceDirect

Construction and Building Materials

journal homepage: www.elsevier.com/locate/conbuildmat

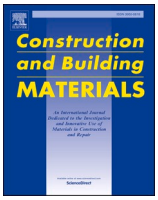

Surface characterization of consolidated earthen substrates using an innovative multi-analytical strategy

Kerstin Elert [a,b,*], Beril Biçer-Simşir [c], Elena Correa [d], Carlos Rodriguez-Navarro [b], Davide Gulotta [c]

[a] Escuela de Estudios Árabes, Consejo Superior de Investigaciones Científicas, Cuesta del Chapiz 22, Granada 18010, Spain
[b] Department of Mineralogy and Petrology, University of Granada, Fuentenueva s/n, Granada 18002, Spain
[c] Getty Conservation Institute, 1200 Getty Center Drive, Los Angeles 90049, USA
[d] Patronato de la Alhambra y Generalife, Junta de Andalucía, C. Real de la Alhambra s/n, Granada 18009, Spain

ARTICLE INFO

Keywords:
Surface hardness
Mechanical properties
Surface wettability
Microstructural changes
Clay minerals
Consolidant penetration

ABSTRACT

This study evaluates the combined use of innovative non-destructive methods and standard laboratory techniques for assessing the surface effects of various consolidation treatments (i.e., bacterial biomineralization, alkaline activation, colloidal dispersions containing nanolime or nanosilica, and ethyl silicate as a standard) on earthen building materials. It demonstrates that novel portable equipment (i.e., portable digital microscope, air permeameter, and mobile surface (contact angle) analyzer) and advanced strategies for the application and data interpretation of conventional analytical and testing methods (i.e., scanning electron and confocal microscopy, Leeb hardness testing, and visible light spectrophotometry) can yield complementary and extremely valuable quantitative results for the evaluation of consolidation treatments on such complex substrates. Our multi-analytical approach allows a detailed characterization of surface and near-surface features of treated earthen mock-ups. It is possible to disclose significant differences in the film-forming propensity and in-depth distributions of consolidants and their effect on key properties such as surface roughness and appearance, permeability, water behavior, and mechanical properties. Even though, the substrate's inhomogeneity and surface texture has proven to be especially challenging, this methodology offers a promising strategy for long-term *in-situ* monitoring of treatment performance and weathering behavior of built heritage materials.

1. Introduction

The complex interplay between chemical and physical weathering processes, both natural and anthropic in nature, represents a serious challenge for the conservation of outdoor-exposed built and sculptural heritage, leading to its degradation and sometimes complete loss [1–5]. Numerous conservation treatments have been developed to mitigate the effects of such degradation phenomena, often involving consolidation treatments. The general working principle of consolidation is to improve surface mechanical cohesion and ultimately reduce material loss. This objective is achieved by forming new cementing phases within the porous system capable of binding loose particles and providing an effective bridging between the weathered superficial material and the more stable substrate underneath. In some instances, a combined approach integrating a protective surface coating can be effectively pursued. Such coatings commonly induce changes in the surface mechanical properties, appearance, permeability, and wettability, involving several chemical and physical processes, thereby preventing, or at least limiting, the access of water into the porous substrate (i.e., water is a main driver for physico-chemical weathering and biodeterioration). Some conservation materials can serve both purposes (surface protection and consolidation), as is the case of alkyl alkoxysilanes [6] and bacterial biomineralization [7]. A vast corpus of knowledge has been produced on the compatibility and performance assessment of consolidation and surface protection treatments for stone [8,9] and references therein]. Little, however, is known about the effects and performance of consolidants applied to earth-based substrates, materials of great relevance to the built heritage with important examples in monumental and vernacular architecture worldwide (e.g., the UNESCO heritage site of Chan Chan, a pre-Columbian city in Peru, the historic city Dejenné in Mali, the Fujian *Tulou* earthen houses in China, or the Alhambra fortress in Spain).

* Correspondence to: Escuela de Estudios Árabes, Consejo Superior de Investigaciones Científicas (EEA-CSIC), Cuesta del Chapiz 22, Granada 18010, Spain.
E-mail address: kelert@ugr.es (K. Elert).

https://doi.org/10.1016/j.conbuildmat.2024.137154
Received 20 March 2024; Received in revised form 2 June 2024; Accepted 17 June 2024
Available online 25 June 2024

Consolidation can be considered an invasive treatment because of its inherently irreversible nature and the resulting impact on the physico-chemical properties of the substrate. Indeed, past inadequate consolidation treatments have proven unsuccessful in reducing weathering, and occasionally even led to accelerated deterioration of earthen structures [10]. The additional challenges posed by the consolidation of earthen substrates when compared to other built heritage materials are linked to the often high content in clay minerals, which act as a binder for the coarser soil fractions but undergo constant volume changes upon moisture variation. This can have devastating effects, especially in the case of expansive clays such as smectites that might double their volume in contact with water, creating swelling pressure >100 N/mm^2 [11]. Experimental evidence has shown that repeated volume changes can cause erosion and reduce the treatment effectiveness over time [12]. Clay swelling can also significantly influence consolidant penetration and ultimate treatment efficacy.

Soil is a comparatively fragile building material and consolidation-related changes in surface properties have rarely been investigated in a comprehensive manner [13–15], even though they control, to a great extent, substrate durability [4]. The surface represents the interface between the material and its environment, and properties such as hardness, cohesion, roughness, permeability, and wettability control physico-chemical weathering processes, which, in most cases, progress from the surface inwards. An in-depth understanding of surface properties and their modification upon consolidation is thus of utmost importance.

Here we investigate the performance of conventional (i.e., a commercial ethyl silicate-based product is included as reference) and more recently developed consolidation methods based on colloidal dispersions containing silica or calcium hydroxide nanoparticles, alkaline activation and biomineralization for the conservation of earthen substrates. Building on previous results from the field application of such treatments for the stabilization of a historic earthen wall at the Alhambra, Granada, Spain [7] that focused on changes affecting the bulk material, here we test an integrated characterization strategy to gain a deeper understanding of surface and sub-surface changes upon consolidation. Our research efforts aim at expanding current testing capacities as the evaluation of fragile and inhomogeneous earthen substrates has proven difficult (i.e., compositional and/or textural inhomogeneity caused by clay- and lime-rich layers in lime-amended rammed earth walls, the presence of large mineral grains, and/or advanced deterioration including granular disintegration and scaling) [7,16]. The main objectives of this investigation are to i) validate the suitability of innovative non-destructive portable methods, some of which rarely applied in the field of built heritage conservation (i.e., air permeameter and mobile surface analyzer), with standard laboratory techniques and ii) advance the application and data interpretation of conventional techniques for the study of consolidation-related surface changes including the use of contact mechanics theory. The portable equipment has been selected based on its capacity to monitor meaningful parameters for the direct assessment of the consolidation effect (e.g., surface hardness) or changes in surface properties with implications for treatment compatibility (e.g., permeability and hydric properties). The outcome of this investigation will not only contribute to a better understanding of surface properties of the earthen substrate and their modification by consolidants, but also provide an advanced strategy for the *in situ* weathering assessment and long-term monitoring of the treatment efficacy of building materials. In addition, practical implications for consolidant applications to earthen substrates useful to specialists working in the field are discussed and further research needs are outlined.

2. Materials and methods

2.1. Sample preparation

Local soil from the Alhambra Formation outcrops (Granada, Spain) was used as the raw material for earthen mock-up fabrication. This soil has historically been used as a building material for rammed earth structures at the Alhambra and Granada's medieval city walls [12]. Considering that the durability of earthen structures is largely controlled by the properties of the clay-rich matrix that acts as a cement for the coarser grains and pebbles, earthen mock-ups (4 cm cubes) were prepared using the <1 mm fraction obtained by dry sieving. Note that in soil science the commonly considered upper limits for the clay, silt and sand fractions are 2 μm, 63 μm, and 2 mm, respectively. According to X-ray diffraction, the soil used in this study is composed of 50–60 wt% clay minerals, 35–40 wt% quartz, ~5 wt% feldspars and small amounts of calcite/dolomite (<5 wt%) as well as iron-oxyhydroxides (i.e., hematite and goethite, <5 wt%), the latter phases being responsible for the reddish-brownish color of the soil. The <2 μm fraction contains smectite and interstratified illite–smectite (expansive clay, 15±5 wt%), illite (45 ±5 wt%), paragonite (<5 wt%), kaolinite (30±5 wt%) and chlorite (<5 wt%), all being common clay minerals and typical soil constituents except for paragonite [7,17,18]. The organic matter content of this soil is 1.1 wt% [17]. Mock-ups (12 per treatment) were manually prepared using wooden frames and a water/soil weight ratio of 0.2. Blocks were dried under laboratory conditions (20±5°C, 40±5 % RH) for two months prior to consolidant application. Note that no attempt has been made to perform *in-situ* testing of earthen structures at this stage of our investigation as a previous study [7] has shown that consolidation-induced effects were often masked by important substrate inhomogeneity, which would have complicated the validation of the non-destructive (portable) techniques tested here. Thus, we opted for the use of more homogeneous earthen mock-ups that serve as a model and provide valuable information for real case scenarios, especially considering the comparative nature of this study.

Several conventional and more recently developed consolidation treatments were selected based on current research trends, only considering inorganic consolidants in order to avoid compatibility issues and/or problems related to biodeterioration or photo-induced degradation (Fig. 1). To date, the application of many of the selected consolidants (i.e., nanolime, nanosilica and biomineralization) has been limited to (mainly) calcareous stone substrates and little is known regarding their consolidation efficacy for earthen substrates. Ethyl silicate was introduced in the 1970s and is the most common consolidant for earthen structures [19]. Once applied to the substrate, this consolidant undergoes hydrolysis and polycondensation to produce an amorphous silica gel. The chemical affinity of the silica gel allows for the formation of siloxane (Si-O-Si) bonds with silicate minerals in the substrate and induces strong cementation [6]. Since its first introduction in 2001, nanolimes (alcoholic dispersions of $Ca(OH)_2$ nanoparticles that carbonate once in contact with ambient CO_2) have found widespread application in heritage conservation [20], and have only recently been tested on earthen substrates [7,13,14]. Note that low-concentrated nanolime dispersions (~5 g/L) are recommended to obtain optimum penetration [21]. However, preliminary tests with diluted dispersions did not lead to improved penetration or reduced color change in the case of the earthen mock-ups of this study (see discussion). Therefore, the commercial product was applied as supplied by the manufacturer (25 g/L). The recently proposed alkaline activation relies on the partial dissolution of clays and other reactive aluminum-silicate phases at high pH (>12) and the subsequent formation of amorphous zeolitic precursors with cementing properties. It consists of repeated applications of a concentrated KOH solution and 1-month curing at high RH (80 %) to enable mineral dissolution and precipitation of cementing phases [22]. About a decade ago, nanosilica (an aqueous colloidal dispersion of silica nanoparticles, which forms silica gel upon drying) was proposed as a

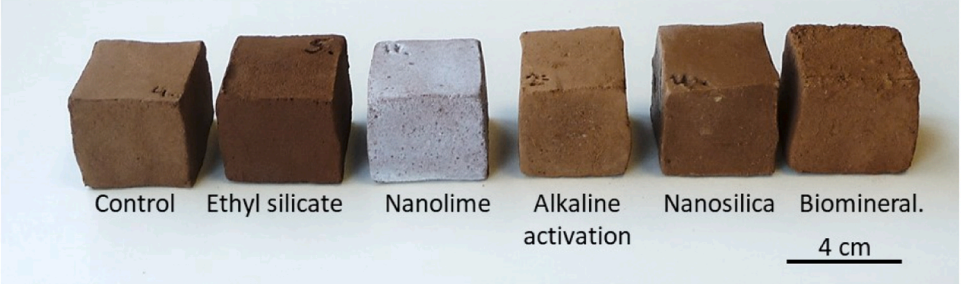

Fig. 1. Photographic image of the earthen mock-ups before (control, CON) and after the application of the consolidation treatments.

stone consolidant [23], but has rarely been applied to earthen substrates [7,24,25]. The biomineralization treatment is based on the activation of indigenous carbonatogenic bacteria in the soil to produce a hybrid cementing material containing calcium carbonate and bacterial-derived exopolymeric substances (EPS, composed of polysaccharides, proteins, DNA, and RNA). This treatment involves repeated applications by spray of the water-based patented M-3 P nutritional solution , followed by curing at high RH to promote bacterial activity and generation of a hybrid cement [26]. The remaining consolidants were applied by brush (see Table 1 for consolidant properties and specific information on application and curing conditions).

2.2. Analytical techniques and testing methods

The distribution of the consolidant on the surface and sub-surface was studied using both surface fragments and 30 μm thick, polished, carbon-coated cross-sections of the treated earthen mock-ups. Elemental maps were obtained with a field emission scanning electron microscope (FESEM, AURIGA, Carl Zeiss, Germany) coupled with energy dispersive X-ray spectroscopy (EDS, INCA-200, Oxford Instruments, UK), working at 10^{-6} Pa vacuum and 20 kV acceleration voltage for backscattered electron (BSE) imaging and microanalysis, and 3 kV for secondary electron (SE) imaging. Additional images and elemental maps were obtained using a Phenom XL scanning electron microscopy (Thermo Scientific, USA) coupled with EDS, working at 0.1 Pa vacuum and 15 kV acceleration voltage for backscattered electron imaging and elemental mapping.

Table 1
Consolidation treatment application and curing in the laboratory.

Consolidant	Label	Applic. method	Total consol. amount (L/m^2)	Curing cond. T (°C), RH (%)	Curing period (days)
Ethyl silicate*	ES	Brush	1.5	20±5, 50 ±5	28
Nanolime**	NL	Brush	0.15	25±5, 80 ±5	28
Alkaline Activation ***	KOH	Brush	0.7	25±5, 80 ±5	28
Nanosilica****	NS	Brush	0.2	25±5, 80 ±5	28
Biomineralization *****	BAC	Spray	1.2	25±5, 80 ±5	14

* Estel 1000 in white spirit D40, used as is, solid content: min. 35 wt% (C.T.S., Spain).
** Calosil E25, 25 g/L in ethanol, used as is, ~150 nm particle size (IBZ-Salzchemie GmbH&Co.KG, Germany).
*** aqueous 2 M KOH solution
**** Nano Estel, solid content: 30 wt%, colloidal silica dispersed in water, used as is, 10–20 nm particle size (C.T.S., Spain).
***** Patented nutritional solution M-3 P containing 1 % [wt./vol.] Bacto™ Casitone (a pancreatic digest of casein), 1 % [wt./vol.] $Ca(CH_3\text{-}COO)_2{\cdot}4\ H_2O$ (total calcium: 43.44 mM), 0.2 % [wt./vol.] $K_2CO_3{\cdot}1/2\ H_2O$ (total potassium: 35.6 mM; total carbonate: 17.8 mM), and 10 mM phosphate buffer in distilled water (pH = 8).

Surface documentation and monitoring of treatment-induced changes were conducted by combining preliminary observations with a portable digital microscope and in-depth investigation using 3D microscopy. Digital microscopy was carried out by a Dino-Lite Premiere digital microscope (Dunwell Tech. Inc., US), with a 5MP resolution, coupled with an external LED diffused white light illuminator to enhance the surface topographical features and allow for consistent lighting conditions. An X-rite color checker was employed for white balancing. A VHX-6000 digital 3D microscope (Keyence Corp., Japan) in visible reflected light mode was employed for complementary observations and to determine the indentation areas and depths after surface hardness testing (see Supplementary Data for additional information and Fig. S1).

The colorimetric characterization of the substrates was carried out with a CM-600D VIS-light spectrophotometer (Konica Minolta, Japan) in the 400–700 nm spectral range, equipped with an 8 mm aperture and a D65 illuminant at 8°. Both SCI/SCE conditions (Specular Component Included/Excluded) were recorded. The complete spectral information was collected, and data were elaborated according to the CIE $L^*a^*b^*$ standard color space [27]. The average values of eighteen measurements per specimen were used to calculate the total color difference ΔE^* ($\Delta E^* = [(L_t^*-L_{CON}^*)^2 + (a_t^*-a_{CON}^*)^2 + (b_t^*-b_{CON}^*)^2]^{1/2}$) between the untreated (*CON*) and consolidated (*t*) substrates.

The surface roughness of untreated and consolidated earthen mock-ups was measured using a confocal microscope (Leica VDM2000, Leica Microsystems, Germany). Leica Application Suite v.3.8.0 and Leica Maps Start v.6 software was used for image processing and data analysis, obtaining 11.3×15.3 mm 3D surface maps as well as roughness parameters including: *Sa* (arithmetic mean height deviation), *Sz* (average peak to valley height), the *Ssk* (skewness, asymmetry of the shape of the area with respect to its mean), and *Sku* (kurtosis, describing the sharpness distribution, a value of 3 being a normal distribution) [28]. Reported average values are based on at least 5 surface maps 3×4 mm in size per specimen.

Air permeability measurements were performed using a portable hand-held TinyPerm3 air permeameter (New England Research, Inc., US), which was originally designed for rock characterization [29] and, so far, has found very limited application in the field of heritage conservation [30–32]. The system is based on the pulse-decay method. Vacuum conditions at the substrate/air interface are created by a single piston stroke that draws air from the substrate. The instrument records the volume of withdrawn air and the transient vacuum pulse, converting the resulting data into a permeability value expressed in Darcy [D]. At least 9 measurements were conducted on untreated and consolidated substrates and an unpaired T-test was used for statistical data analysis.

The total pore volume and pore size distribution of the 5 mm thick outermost surface layer of earthen mock-ups before and after consolidation were determined with mercury intrusion porosimetry (MIP) using an Autopore III 9410 porosimeter (Micromeritics, Norcross, US), which measures pores with 0.003–360 μm diameter. Prior to analysis,

samples (~1.5 g) were dried in an oven with forced ventilation for 48 h at 60 °C until constant weight was reached. Analyses were performed in duplicate.

Surface hardness (HLC) measurements were conducted under controlled *T*- and *RH*- conditions (20 °C, 40 % *RH*) following the dynamic rebound testing method according to Leeb [33–35], using an Equotip 550 device (Proceq, Switzerland) with a C-type probe and 3 Nmm impact energy. This method was originally developed for testing metal surfaces [33,34] and recently adapted for rock characterization [36] and weathering studies of heritage materials [37]. Measurements were randomly distributed across the untreated and consolidated substrates following the Single Impact Method [38]. As the sampling size plays a critical role for a reliable interpretation of the collected data [37], at least 70 rebound values were recorded for each substrate and an unpaired T-test was used for statistical data analysis.

To gather further information on the mechanical properties of the indented surfaces (before and after consolidation) we analyzed the geometry (diameter, projected area, and depth, determined using 3D microscopy, see Supplementary Data) of the indentation marks left on the substrates after surface hardness measurements using contact mechanics theory [39]. With some limitations (see below), this analysis enables determining the reduced modulus E_r and indentation hardness H in an analogous way as it is determined using instrumented micro- and nanoindentation [40]. Considering the mass m of the spherical indenter (3.1 g) and the impact (kinetic) energy, E_k (0.003 J), an impact velocity v of 1.394 m/s is calculated using E_k=0.5 mv^2. This yields a peak force or maximum indenter load P of 6 N, for a contact length of 1 mm (consistent with the impact energy of the indenter). E_r for the spherical indenter was calculated using the Hertz contact model [39,41], which gives the following relationship between E_r, the applied load P, the indenter radius R, and the resulting indentation depth h:

$$E_r = \frac{4P}{3\sqrt{R}h^{\frac{3}{2}}} \quad (1)$$

It should be noted that Hertz's analysis was developed for an elastic response [41]. However, this analysis is a good approximation for both the static and dynamic interactions of hard indenters with a range of materials showing elasto-plastic behavior and displaying yield stress [42]. Because earthen materials display an elasto-plastic behavior [43–45], we calculated the effective radius R_e to be used in Eq. (1) by measuring the radius r of the projected surface area of the indentation mark (see above), and its depth h_c, using the following equation [46]:

$$R_e = \frac{r^2 + h_c^2}{2h_c} \quad (2)$$

The reduced modulus depends on the Young's modulus and Poisson ratio of the indented material (E and ν) and the indenter (E_i and ν_i) as given by:

$$\frac{1}{E_r} = \frac{(1-\nu^2)}{E} + \frac{(1-\nu_i^2)}{E_i} \quad (3)$$

As the modulus and Poisson ratio of the indenter are known (E_i=696 GPa, ν_i=0.21), Eq. (3) enables determining E for indented materials with known Poisson ratio. In our case, however, the exact Poisson ratio of porous polymineralic mock-ups is unknown. Therefore, we considered the often reported 0.22±0.01 Poisson ratio for earthen materials [43,45]. Note, however, that measured h_c values (3D microscopy analysis, see Supplementary Data) do not correspond to the maximum h value reached at peak force, but rather to the permanent plastic deformation resulting from the indenter impact. Although we used an effective value of R_e to account for plastic deformation, this means that the calculated E values are probably overestimated. This is not necessarily a shortcoming of this approach as we strive to disclose the relative variations in E induced by the different treatments.

H values were determined using the following equation (for a spherical indenter) [39,40]:

$$H = \frac{P}{A} \quad (4)$$

where A is the projected area of the hemispheric indentation mark. Note that it has been shown that the lateral deformation of the indented body during the unloading stage is negligible (i.e., the projected area of the indenter impression after unloading corresponds to the projected area at maximum load) [40]. Unlike the case of the approach used to estimate E, the determination of H is not subjected to any ambiguity, and errors associated with this measurement are only associated with the measurement of the indentation area A.

Surface cohesion of earthen mock-ups was evaluated using the peeling or "Scotch tape" test [47], which compares the mass (g) per unit area of removed material from the untreated and consolidated surface by a sticky tape. For testing, 3×3.8 cm adhesive tape stripes were applied by gently pressing them against the surface with the thumb. Reported values (normalized to g/m^2) are based on four tests per sample. An unpaired T-test was used for statistical data analysis.

Surface wettability properties were assessed by measuring water contact angle and micro drop absorption times of untreated and consolidated substrates. A mobile surface analyzer (MSA, Krüss GmbH, Germany), was used to dose 4 µL drops of distilled water onto the surfaces. This instrument was designed for different technical applications, including the quality control of metals, textiles, polymers, and glass coatings [48,49], and to the best of our knowledge, its application to built heritage research has not been systematically reported so far. In addition to its portability, this instrument provides flexible measuring conditions, allowing for the analysis of both horizontal and vertical surfaces. At least 3 repeated measurements were acquired with horizontal orientation. Average absorption times and contact angle values were calculated from video recordings acquired at 10 fps. An unpaired T-test was used for statistical data analysis.

3. Results

3.1. FESEM analysis of surface fragments and cross-sections

Alkaline activation (KOH) has a limited effect on the mock-ups' surface features and only scarce formation of a gel-like phase is detected (probably an amorphous zeolite precursor with cementing capability [22]), partially covering the soil particles (Fig. 2a). These findings are in line with previous X-ray diffraction results [7], which only showed negligible changes in the overall mineralogical composition of rammed earth after alkaline activation, supporting the assumption regarding the amorphous character of the newly formed phases. FESEM-EDS elemental mapping of cross sections of the earthen mock-up treated with alkaline activation suggests the presence of potassium-rich phases in direct contact with poorly crystalline aluminosilicates. According to FESEM-EDS (Fig. 2b, EDS in inset), these phases have a chemical composition close to that of zeolite K-I and K-F ($KAlSiO_4{\cdot}2\ H_2O$ and $KAlSiO_4{\cdot}1.5\ H_2O$, respectively). These types of zeolites have been previously synthesized using 1.8–4.0 M KOH solutions and various clay minerals [50]. Detected potassium-rich phases could thus correspond to zeolitic precursor, formed as a result of consolidant-substrate interactions upon alkaline activation, which, however, did not lead to increased mechanical strength even though an improvement in water resistance was obtained according to previous results [7].

Bacterially treated mock-ups (BAC) show minimal changes in surface texture. However, the presence of a limited amount of EPS, which is unevenly distributed, spreading over soil particles and partially bridging the interparticle space (Fig. 2c, solid white arrows), as well as calcified bacteria cells (Fig. 2d, inset, solid white arrows) provides clear evidence for successful bacterial activation. Indeed, previous culturable bacteria count revealed an almost 4 orders of magnitude increase from 6.59 ± 1.20 × 10^3 colony forming unit (CFU)/g before treatment to 2.10 ± 0.04

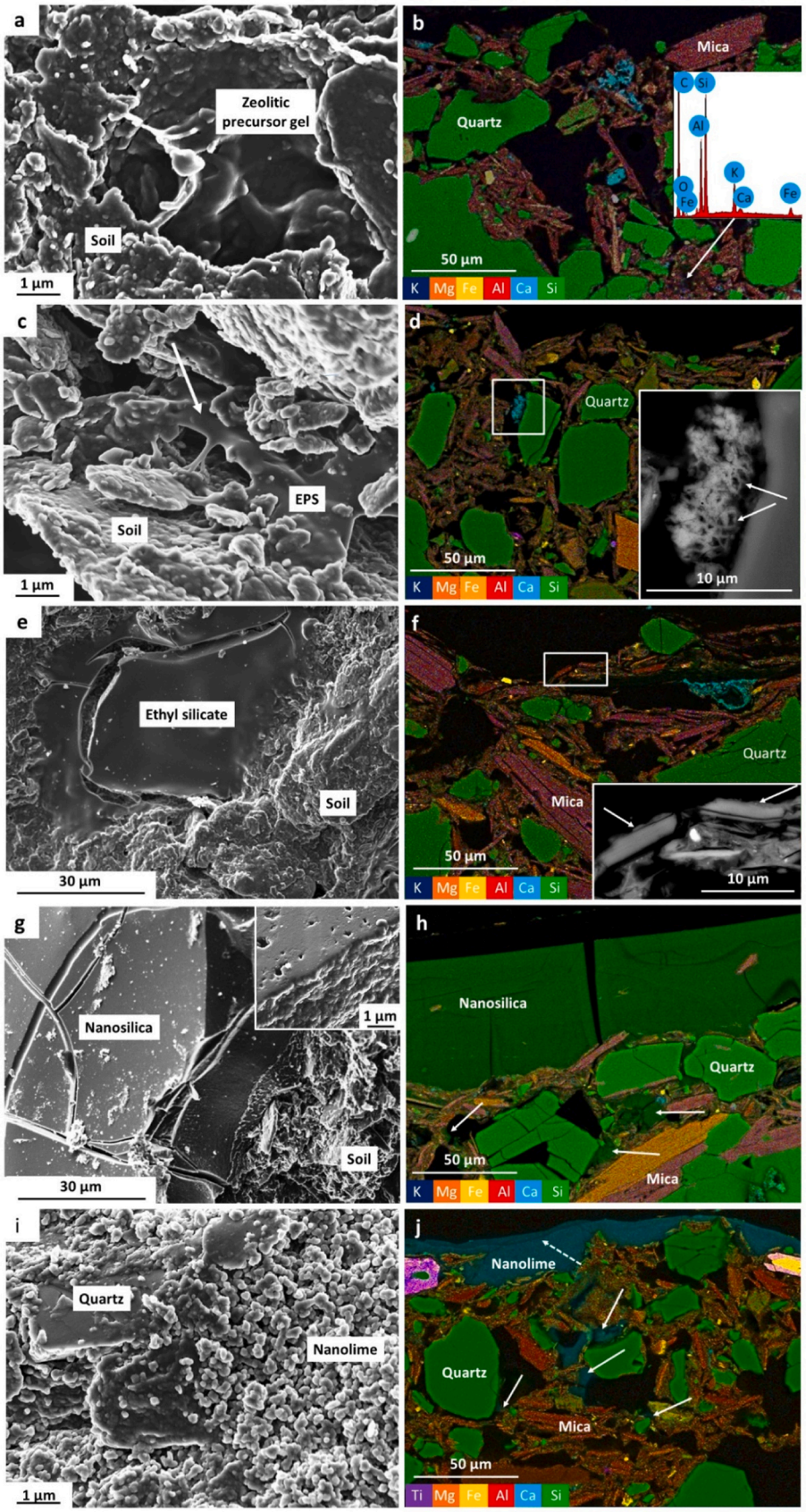

(caption on next page)

Fig. 2. FESEM secondary electron images of surface fragments (left panels) and elemental maps of cross-sections (right panels, the treated surface always being aligned along the top of the image) of earthen mock-ups treated with: a) and b) KOH, showing the formation of a gel-like phase, probably an amorphous zeolitic precursor (EDS analysis in inset); c) and d) BAC, showing EPS bridging mineral grains (white arrow) and scarce formation of cement containing calcified bacteria cells (BSE image in inset, white arrows); e) and f) ES, showing consolidant accumulation with crack formation and a few hundred nanometer-thick silica-gel coating on mineral grains at high magnification (BSE image in inset, white arrows); g) and h) NS, showing a ~60 μm thick surface layer with crack formation and some pore filling (white arrows) and detail of the consolidant layer formed by silica nanoparticles in inset; and i) and j) NL, showing the formation of an almost continuous ~20 μm thick calcite surface coating (different application layers can be distinguished, dashed white arrow) and scarce pore filling up to ~100 μm depth (solid white arrows).

$\times 10^7$ CFU/g after treatment [7]. Despite the increased bacterial activity, the cross-section only shows a very limited amount of bacterial calcium carbonate cement, unevenly distributed within the porous substrate (Fig. 2d). Previous thermogravimetric analyses are consistent with these findings, revealing a relatively small increase in calcium carbonate (~6 wt%) and organics content (0.5 wt% corresponding to bacterial EPS and cells/debris), being consistent with a relatively limited improvement in mechanical strength and water resistance [7].

Silica gel development following ethyl silicate (ES) application generally results in little modification of the original textural surface features as most of it is absorbed by the porous substrate. However, typical cracking associated with shrinkage of the gel during solvent evaporation and polycondensation is detected where local consolidant accumulation occurred in valleys between mineral grains (Fig. 2e). The cracks are caused by the extremely large capillary forces generated in very small pores (3–10 nm) upon drying of the amorphous gel [51]. FESEM-EDS elemental maps do not provide clear evidence for the presence of the ethyl silicate coating or massive pore filling, but BSE imaging of the cross-section enables the identification of a few hundred nanometers thick consolidant film covering some of the mineral grains (Fig. 2f, inset, solid white arrows).

The colloidal nanosilica (NS) dispersion forms a relatively thick (~60 μm) compact film that homogeneously covers surface valleys and peaks and displays a network of micro-cracks (Fig. 2g and Fig. S2b, Supplementary Data). The original surface textural features of the substrate can only be observed where the silica gel layer is missing or has a discontinuous distribution. High-resolution FESEM observations show that the consolidant layer is made up of silica nanoparticles (10–20 nm in size, according to the manufacturer) and has nanosize pores in the gel surface (Fig. 2g, inset). Newly formed amorphous silica gel can be differentiated by EDS analysis within the porous substrate from quartz grains by its darker shade of green (false color corresponding to Si in Fig. 2h, solid white arrows), detected up to 150 μm in depth. Such limited penetration is in line with the results of previous studies, showing a penetration depth of ≤1 mm in fairly porous ignimbrite and lime mortar [52,53].

The original surface texture of nanolime-treated mock-ups is concealed to a great extent due to an almost continuous surface layer of densely-packed nanometric (i.e., ~150 nm in size) calcite crystals (Fig. 2i). Calcite formed upon carbonation of the original portlandite ($Ca(OH)_2$) nanoparticles following an interface-coupled dissolution-precipitation process [54]. The film varies in thickness, reaching up to ~25 μm in valleys but only a few micrometers on peaks. BSE imaging of a cross-section allows the differentiation of several nanolime application layers (Fig. 2j, dashed white arrow; Fig. S2a, Supplementary Data). Indeed, the formation of a whitish veil was visually detected right after the application and limited further consolidant uptake. These observations suggest that, in this case, back migration was not responsible for the relatively thick surface coating as it has been reported for other substrates, such as nanolime-treated sandstone [55]. In addition, scarce patches of nanolime are detected in subsurface zones, which are limited to a very thin surface layer <100 μm in thickness. Poor penetration and the formation of a surface layer have been previously reported by Michalopoulou et al. [56] in the case of clay-rich mudbricks treated with alcoholic nanolime dispersions and reported penetration depth hardly ever exceeds a few millimeters in materials with small mean pore size [57–59].

3.2. Portable digital microscopy and spectrophotometric measurement

Considering the generally accepted limit of detection of color changes by the human eye ($\Delta E^*>3$) and threshold for the aesthetic compatibility of conservation treatments ($\Delta E^*<5$) [60,61], KOH and BAC treatments can be considered fully compatible under the aesthetic point of view. Compared to the untreated sample (Fig. 3a), total color change values are, in both cases, lower than 2 units and the overall spectral data confirm the absence of any significant alteration of the reflectance patterns upon treatment (Fig. 3b and c). Digital microscopy images show that the original surface texture and topographical features (Fig. 3b and c, insets and Fig. S3) are largely preserved as well, and the somewhat increased surface roughness (see Section 3.3.) resulted in only a minor increase in luminosity.

The intense color change associated with ES application is mostly due to variation in lightness, a well-known drawback of this type of treatment [6,7], although the spectral features are mostly preserved. The overall shift of the reflectance curve toward lower values and the reduced saturation of the b^* coordinate are indicative of a darker substrate with a colder hue (Fig. 3d). Microscopy images reveal no important changes in surface appearance of the substrate (Fig. 3d, inset), even though a reduction in reflectance is caused by the filling of pores with the silica gel consolidant, which has a higher refractive index (1.38 and 1.30 for silica gel with 25 % and 40 % porosity, respectively) as compared to air (1.00) [62].

A highly cracked glass-like superficial layer is observed after NS consolidation, clearly altering the overall appearance of the treated substrate (Fig. 3e, inset). The main effect of the NS application is an increase in surface gloss, as indicated by the higher ΔE^* value detected when the specular reflection component (SCI) is factored in, 2.3 units, instead of 1.7 when only SCE values are considered. A significant difference between SCI and SCE values is only detected in the case of NS, as this consolidant creates a relatively smooth coating with surface features smaller in size than the wavelength of visible light, thus promoting specular reflection. In the case of the remaining samples with more pronounced surface roughness, the diffusely scattered light component controls surface appearance and SCI and SCE values are almost identical [63]. In any case, the total color change can still be considered acceptable according to the compatibility threshold, but the negative values registered as a result of the treatment-induced changes along the a^* and b^* color coordinates and a flattened spectral curve are indicative of reduced color saturation of the NS-treated substrate.

The NL application induces the most visible changes in surface features and color (Fig. 3f, inset). The surface accumulation of the consolidant results in a white layer, unevenly covering the substrate. Lanzón et al. [58] presented microscopic images of a nanolime-treated adobe surface with a very similar appearance. The resulting color change observed in this study significantly exceeds the compatibility threshold, being caused by a dramatic increase of the lightness value and the desaturation of the originally reddish substrate, as indicated by the negative shift of both color coordinates upon treatment.

3.3. Confocal and 3D microscopy for the evaluation of surface roughness

Compared with the untreated sample (Fig. 4a), roughness parameters of mock-ups treated with KOH (Fig. 4b) and BAC (Fig. 4c) show limited changes due to material loss induced by the application of these

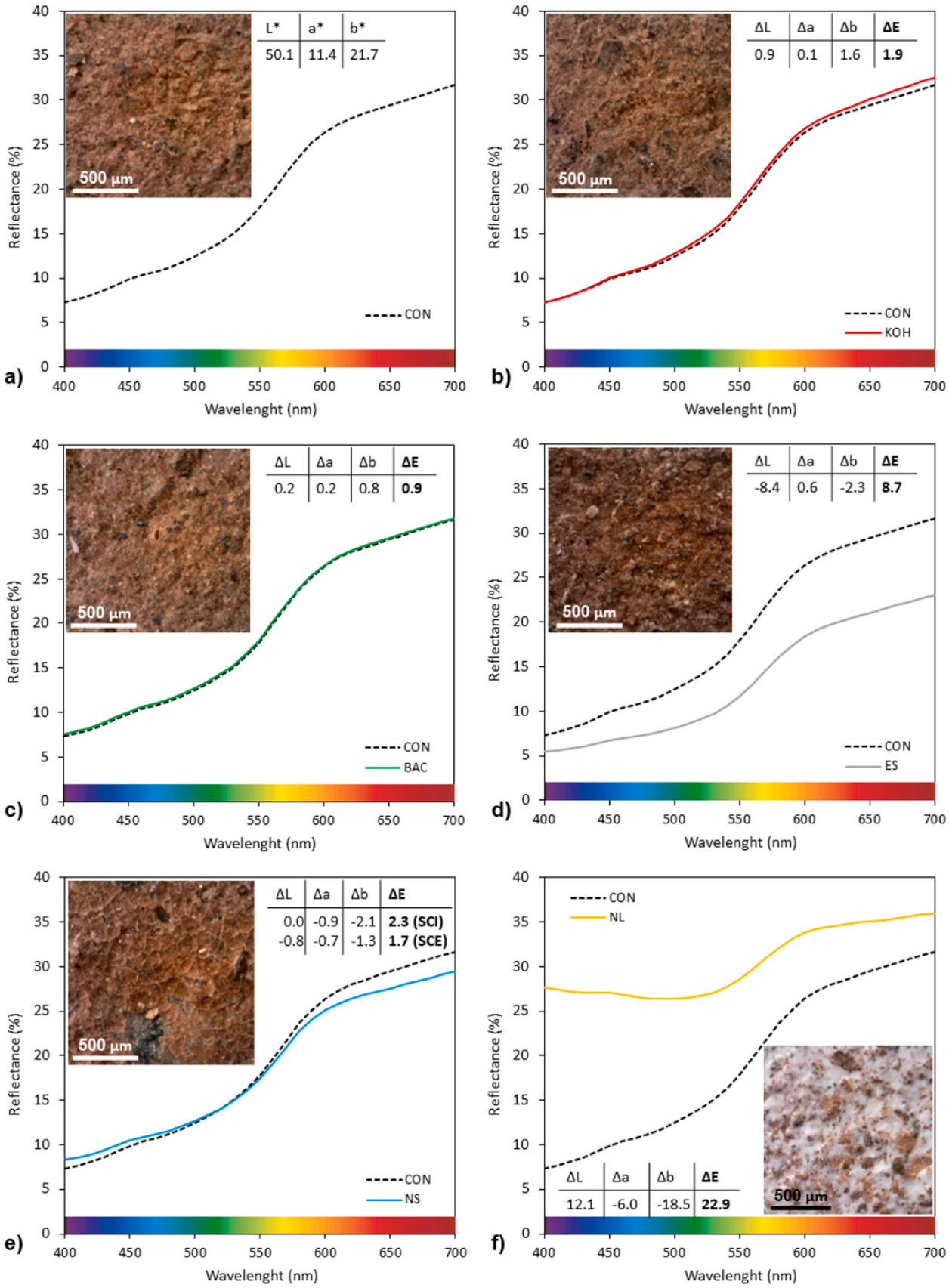

Fig. 3. Reflectance spectra obtained from VIS-light spectrophotometric measurements (all spectra acquired under SCI condition) of reference specimens (dashed black line) and after treatment (solid lines). a) untreated (CON), b) alkaline activation (KOH), c) biomineralization (BAC), d) ethyl silicate (ES), e) nanosilica (NS), and f) nanolime (NL). Insets show the corresponding CIEL*a*b* color parameters and surface features documentation obtained via portable digital microscopy.

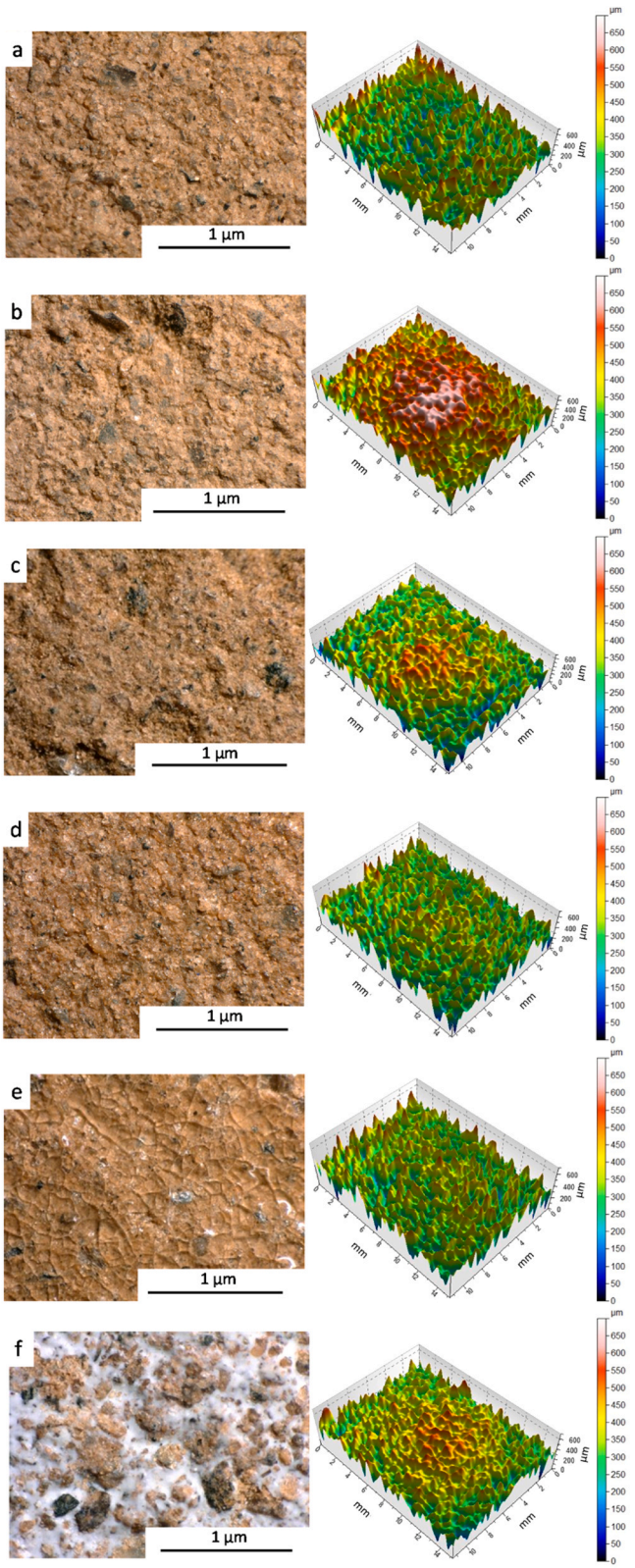

Fig. 4. Microscopy images acquired via portable digital microscopy (left column) and 3D surface maps via confocal microscopy (right column) of earthen mock-ups. a) Untreated (CON), b) treated with KOH and c) BAC, d) consolidated with ES, e) NS, and f) NL.

water-based consolidants. However, the mechanical impact of the brush during the application of the aqueous KOH solution mainly affected the larger and more loosely attached surface grains, and the resulting leveling effect is reflected in a small decrease in Sa and Sz (Table 2). In the case of the BAC treatment, in contrast, surface roughening is observed. The spray application of the aqueous nutritive solution has an erosive effect on the soil matrix. Washing off the fine fraction increases the valley depth, as confirmed by the slightly higher Sz and Sa values as compared to the reference surface (Table 2). ES (Fig. 4d) does not provoke any material loss upon application and is mostly absorbed by the porous substrate. However, the previously mentioned patchy accumulations in valleys have a smoothing effect and result in a decrease in Sa and Sz as compared to the untreated surface (Table 2). In the case of NS (Fig. 4e) and NL (Fig. 4f), material loss upon application was negligible. The former forms a continuous film covering valleys and peaks, having a leveling effect which leads to a 15 % decrease in Sa but does not cause an important reduction in the Sz value. In the case of NS, the average peak-to-valley height (Sz) remained basically unchanged due to substantial crack formation in the silica gel film, which creates additional relatively deep valleys as evidenced by FESEM (Fig. 2g). NL (Fig. 4f) is most effective in decreasing surface roughness (25 % reduction) as it accumulates in valleys but leaves higher peaks largely uncovered, resulting in the lowest Sa and Sz values among all earthen mock-ups (Table 2).

All treatments lead to a decrease in the Ssk value (Table 2), which is, however, insignificant in the case of the ES-consolidated blocks. The Ssk value informs on the symmetry of the height distribution; negative values suggest an increase in asymmetry due to the predominance of deep valleys [64]. In this respect, the mechanical impact of the brush (KOH) and water spraying (BAC), as well as crack formation in the case of NS have to be considered. The former leads to a reduction in peak height/number of peaks (Table 2), while the latter two result in deeper valleys, either due to erosion by water spraying or caused by an increased number of deep valleys due to crack formation in the consolidant layer [65] (Fig. 2g and h, and Fig. S2a and b, Supplementary Data). Sku describes the distribution sharpness, higher values (Sku>3) being associated with steeper peaks and valleys as opposed to more rounded features leading to lower Sku values (Sku<3) [66]. All treatments caused an increase in the Sku values closer to a Gaussian distribution (Sku=3). Only the mock-up consolidated with NS reached a slightly positive Sku value, likely due to the aforementioned presence of disproportionately deep valleys caused by the extensive formation of cracks with a depth of ~50 µm (Figs. 2e and 4e).

3.4. Porosity, density and air permeability

Mercury intrusion curves reveal no important changes in the overall pore size distribution upon consolidation, all samples showing an unimodal distribution with a maximum at 2.2–2.4 µm pore diameter. However, samples treated with KOH have a slightly larger volume of pores ≤1 µm (Fig. 5a), which could be related to flocculation (i.e., decrease in clay particle repulsion in the presence of an electrolyte) induced by the concentrated KOH solution, resulting in the formation of additional pores [12]. A significant reduction in porosity is only

Table 2
Measured surface roughness parameters (including standard deviations) of untreated (CON) and treated earthen mock-ups.

Parameter	CON	KOH	BAC	ES	NS	NL
***Sa* (µm)**	58.0 ±1.4	55.6 ±4.6	60.4 ±4.7	48.1 ±2.0	49.9 ±1.1	43.5 ±2.4
***Sz* (µm)**	419 ±17	388±34	428±36	347±32	395±21	333±22
***Ssk* (-)**	0.04 ±0.05	-0.22 ±0.24	-0.36 ±0.10	-0.06 ±0.11	-0.35 ±0.15	-0.17 ±0.09
***Sku* (-)**	2.59 ±0.15	2.84 ±0.19	2.99 ±0.19	2.75 ±0.16	3.16 ±0.16	2.81 ±0.21

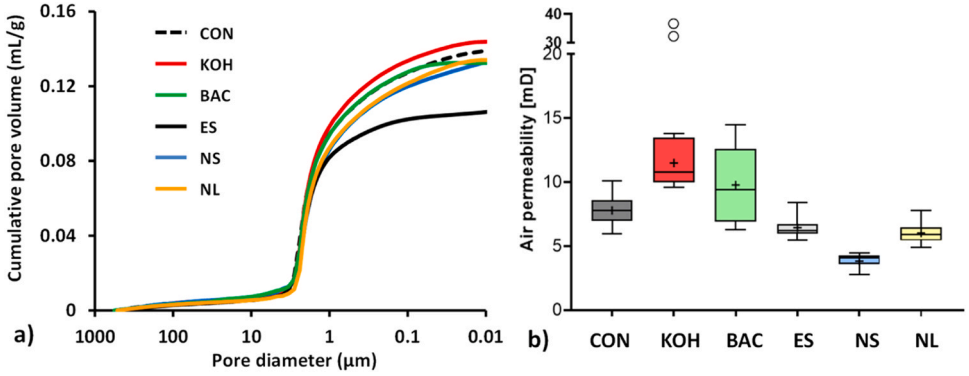

Fig. 5. Cumulative pore volume curves (a) and boxplot summarizing air permeability (b) of untreated (CON) and consolidated earthen mock-ups (Each box extends from 25th to 75th percentiles, whiskers indicate lower/higher absolute values, central line and cross indicate median and average values, respectively. Empty circles indicate outliers).

observed in samples treated with ES (Table 3), mainly caused by the filling of capillary pores with a diameter ≤1 µm, which decreased by 27 % as compared to the untreated control (Fig. 5b). Aqueous KOH and nutritional M-3 P solutions generally show adequate penetration (>2 cm), but do not significantly alter substrate porosity [22,67]. The film forming treatments (colloidal NS and NL dispersions) result in a very limited porosity decrease of 4–5 % as they only penetrated the outermost surface layer according to FESEM observations (Fig. 2g and j, Fig. S2a and b, Supplementary Data) and previous drilling resistance (DR) results [7], thus having little effect on the porosity of the bulk material. Apparent and skeletal density values based on MIP measurements (Table 3) generally show little variations, the latter being coherent with skeletal density values reported for common soil minerals including clays (2.40–2.80 g cm^{-3}), quartz (2.62 g cm^{-3}), feldspars (~2.70 g cm^{-3}), and carbonates (2.70–2.85 g cm^{-3}). The apparent density of ES-treated samples is slightly higher due to the partial filling of pores with silica gel as evidenced by the reduction in porosity, which affected the entire cube. Indeed, DR measurements prove the exceptional penetration capability of ES with a drilling resistance increase along the entire 2 cm drilling profile [7].

Increased air permeability values are detected after the water-based KOH and BAC treatments (Fig. 5b), which in the case of the former treatment is likely related to the increased volume of pores with ≤1 µm diameter, detected with MIP (Fig. 5a). In the case of BAC treated samples, the large data spread suggests important material inhomogeneity that precludes a definitive interpretation of the air permeability data. ES and the film-forming treatments (NS and NL), conversely, show reduced values. The most intense reduction effect (i.e., 50 % reduction considering the mean value) is caused by the NS treatment, which is consistent with the formation of a superficial, and less air-permeable, silica gel layer (Fig. 2f, Fig. S2b). Remarkably, substantial crack formation did not cancel out such sealing effect, likely due to the observed crack narrowness. A significant reduction in air permeability due to the sealing of surface pores, as observed here for the case of the NS treatment, is problematic since it may foster further damage to the substrate through the creation of an impervious barrier [8]. Previously reported water vapor transmission rate (WVTR) data [7] using 5 mm thick surface slabs (Table 3) revealed a clear reduction of 35 % only in the case of ES-treated samples, while this testing method was not able to detect superficial pore sealing in NS-treated samples [7]. This finding shows that WVTR testing provides valuable indications regarding the overall permeability of the bulk material, but, in contrast to air permeability measurements, might not be able to detect changes only affecting very thin surface layers.

Table 3
Total porosity φ (%), apparent density ρ_a (g cm^{-3}) skeletal density ρ_e (g cm^{-3}) and water vapor transmission rate WVTR (g m^{-2} day) of untreated (CON) and consolidated earthen mock-ups, standard deviation being included [7].

Parameter	CON	KOH	BAC	ES	NS	NL
φ	26.6 ± 0.6	26.9 ± 0.7	24.8 ± 0.7	20.7 ± 0.8	25.4 ± 0.7	25.6 ± 0.7
ρ_a	1.84 ± 0.02	1.86 ± 0.03	1.87 ± 0.03	1.98 ± 0.04	1.86 ± 0.02	1.91 ± 0.02
ρ_e	2.49 ± 0.05	2.55 ± 0.01	2.49 ± 0.02	2.51 ± 0.03	2.50 ± 0.02	2.56 ± 0.03
WVTR	177.1 ± 9.3	157.6 ± 14.2	161.7 ± 3.1	116.7 ± 0.8	192.1 ± 3.3	173.6 ± 5.6

3.5. Surface cohesion and hardness

Peeling test results (Fig. 6a) revealed an improvement in surface cohesion in the case of NL, NS, and especially ES, while BAC and, in particular, KOH, led to reduced values. These findings confirm FESEM observations (Fig. 2b and c) showing very limited formation of cementing phases within the surface layer of the treated earthen mock-ups for the latter treatments, which explains the lack of improvement in surface cohesion. Apparently, the water-based treatments reduced surface cohesion and mineral grains could easily be removed by the adhesive tape. In this respect, flocculation of particles constituting the clay matrix has to be considered as a possible cause for the observed loss of cementation of such grains. Extensive cementation in the case of the ES-consolidated samples, in contrast, improves surface cohesion as indicated by a 90 % reduction in material loss. Film-forming treatments (colloidal NS and NL dispersions) are also quite effective in improving cohesion, resulting in a 50–60 % reduction in material loss, findings which are in line with data reported by Lanzón et al. [58] and Garcia-Vera et al. [13] who detected a reduction in material loss of 60–94 % in the case of nanolime/ethyl silicate-treated adobe and clay-rich plaster.

Leeb surface hardness (HLC) results are generally characterized by remarkable data dispersion, despite the high number of repeated measurements acquired for each condition (Table 4 and Fig. 6b). Nonetheless, the method can discriminate between the surface effects induced by the different consolidation strategies. Changes in Leeb surface hardness resulting from BAC and NL consolidation are very small, whereas a limited strengthening effect is detected after KOH and NS application. In the latter case, the relative increase in the average HLC value as compared with the reference (CON) can be explained considering that NS forms a silica gel surface film that underwent, however, massive cracking upon indentation, as shown by the surface profile obtained via 3D microscopy (Fig. 7). Cracking is associated with the fragile-elastic behavior of silica gel (see below) that limits (permanent) plastic deformation, resulting in a less marked reduction in kinetic energy during the rebound phase and an increase (yet limited) in rebound speed. ES, in

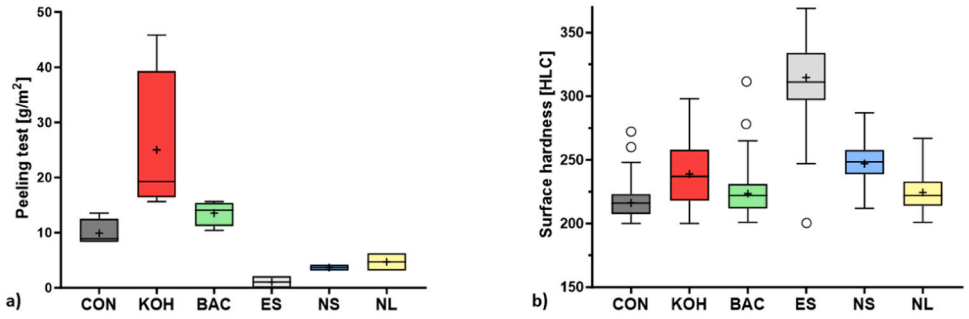

Fig. 6. Boxplots summarizing weight loss (g/m^2) based on peeling test results (a) and surface hardness (b) of untreated (CON) and treated earthen mock-ups. (Each box extends from 25th to 75th percentiles, whiskers indicate lower/higher absolute values, central line and cross indicate median and average values, respectively. Empty circles indicate outliers).

Table 4
Mechanical properties of untreated and treated earthen mock-ups. The elastic modulus (*E*) and indentation hardness (*H*) determined using the contact mechanics model, as well as the values of Leeb hardness (*HLC*), dynamic elastic modulus (E_d), uniaxial compressive strength (*UCS*) and yield strength (*Y*) are presented, standard deviation being included.

Samples	*E* (MPa)	*H* (MPa)	*HLC*	E_d (MPa)	*UCS* (MPa)	*Y* (MPa)
CON	311 ± 10	23.5 ± 0.5	216 ± 11	1693 ± 168	1.0 ± 0.22	70.5 ± 1.5
KOH	303 ± 13	23.3 ± 0.8	239 ± 27	1367 ± 276	1.3 ± 0.11	69.8 ± 2.4
BAC	320 ± 11	27.5 ± 0.4	224 ± 16	1927 ± 268	1.23 ± 0.10	82.6 ± 1.2
ES	1020 ± 107	55.1 ± 4.6	315 ± 26	2302 ± 365	3.54 ± 013	165.0 ± 13.8
NS	307 ± 48	25.2 ± 2.3	248 ± 16	1273 ± 157	1.04 ± 0.18	69.5 ± 6.9
NL	478 ± 69	29.1 ± 3.9	224 ± 15	2052 ± 255	1.02 ± 0.11	87.4 ± 11.7

contrast, marks a clear improvement in surface hardness as compared to the reference substrate, leading to a 45 % increase in the average HLC value. Importantly, previous drilling resistance measurements showed similar trends [7], indicating a substantial increase in drilling resistance in ethyl silicate-consolidated samples especially over the first 6.5 mm (i.e., from 0.9 ± 0.4 N in the untreated sample to 12.2 ± 2.6 N in the ES-treated sample) and a smaller increase (i.e., up to 2.7 ± 0.4 N) restricted to the first 0.6 mm in the case of NS-treated samples [7]. The remaining samples did not experience any important increase in drilling resistance, considering the relatively high data spread. Bearing in mind that rebound hardness is mainly influenced by elastic properties, while drilling resistance is controlled by the material's ability to withstand abrasion, it can be concluded that ES is the only consolidant that improves both. Indeed, the remaining earthen mock-ups show substantial plastic deformation upon rebound testing (Fig. 7).

3D microscopy and surface roughness analysis (Fig. 7) show some morphological differences of the indentation marks among the tested samples, with marked piling up in the control, as well as BAC and KOH treatments, a less marked piling up in the case of ES and NL, and near absence of piling up in the case of the NS treatment. Apparently, the latter treatment suffered limited plastic deformation. Moreover, as indicated above, pervasive cracking (i.e., higher crack density in indentation marks than in the surrounding areas), indicative of brittle fracturing, was observed in the case of the NS treatment, where the limited plastic deformation led to a higher rebound speed and, consequently, higher HLC values than those of the control.

Table 4 shows *E* and *H* values for the control and treated earthen specimens. It is important to underline that despite the shortcomings of the approach (see Materials and Methods), obtained *E* values for earthen mock-ups are in very good agreement with *E* values reported for unreinforced/unstabilized rammed earth and adobe bricks/masonry, which typically range between 50 and 1100 MPa [43–45,68], although a few higher values of up to 4200 MPa have been reported [69], which do not seem to be representative. In addition, a linear correlation between HLC values and *E* values is determined here (Fig. 8a), with a correlation coefficient very similar to that observed for the correlation of HLC and compressive strength (uniaxial compressive strength (UCS) data from Elert et al. [7]) of the tested samples (Fig. 8b, Table 4). There are, however, two aspects that need to be clarified: (i) HCL values (as well as modulus and surface hardness values calculated from indentation) correspond to the surface layer of the samples whereas UCS is a bulk property. Although the KOH and BAC treatments improved UCS to a minor degree, only the ES treatment had a statistically significant impact on UCS and HCL, being the consolidant that affected the strength of the entire bulk material and causing the formation of a hard surface crust [7]. The UCS values of the other treated samples do not show a consistent correlation with HCL values; and (ii) the limited number of data points and their skewness cast some doubts on the reliability of the correlation coefficients determined here. Therefore, the correlations presented in Fig. 8 can only be considered in qualitative terms (i.e., they show tendencies, but not absolute values). Despite these limitations, our results suggest that the used approach to calculate mechanical parameters of earthen materials is valid, as a positive linear (or exponential) correlation for *E* vs. HLC and HLC vs. UCS has been reported for a range of natural rocks and building materials [36,37,70]. *H* values also show a linear correlation with HLC values (with the limitations indicated above) (Fig. 8d). Interestingly, both NL and BAC treatments induce a higher *H* increase than expected from the HLC measurements, underlining that these two parameters do not measure the exact same mechanical properties. Apparently, the two treatments resulted in a relative increase in surface hardness without a parallel increase in the substrate elastic behavior. Conversely, the KOH treatment and, in particular, the NS treatment yield lower *H* values than expected considering their relatively high HLC values. In the first case, the limited surface cohesion (reflected by the high mass loss during the peeling test) might explain this effect. However, in the case of the NS treatment, this inconsistency seems to be related to the formation of a silica gel surface layer, of relatively low hardness. Measured *H* values are orders of magnitude below those reported for common construction materials such as mortars or stones [71], and there is no possibility to compare them with earthen materials, because to our knowledge no *H* values for the latter materials have been reported. Still, we observed an average *H/E* ratio (also known as elasticity index, I_E) of 0.07±0.01, being in good agreement with reported *H/E* ratios for a range of biological materials, such as wood, enamel or calcite shells, with average values of 0.05 [72] and building materials such as lime mortars with a value of 0.065 [71]. These results also show that the approach used here to calculate *E* and *H* is robust.

For comparison purposes, we also considered the use of a dynamic contact model involving deformation following impact of a hard sphere

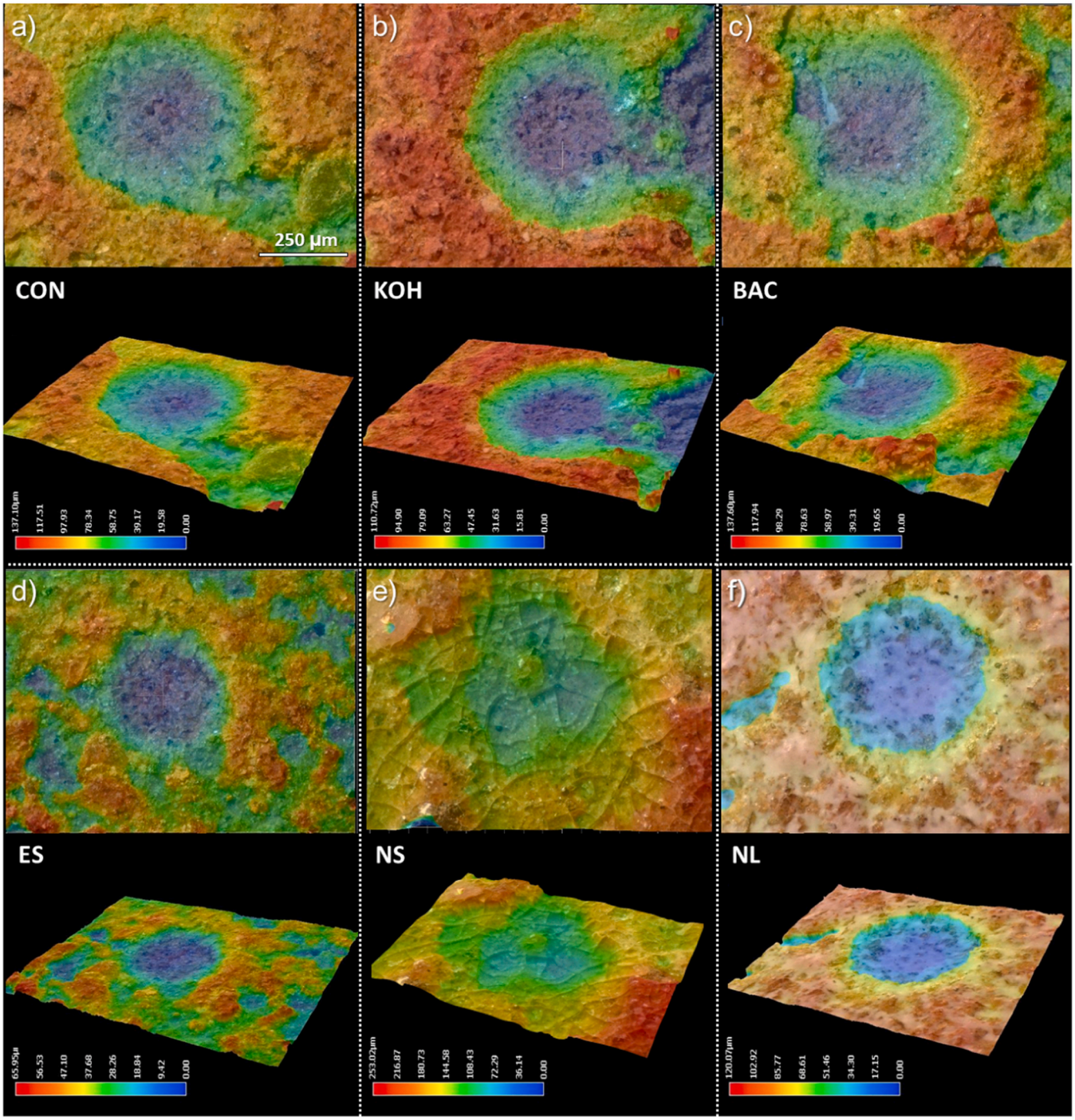

Fig. 7. 3D microscopy and surface roughness analysis of indentation marks on the earthen mock-ups. a) Untreated sample (CON), b) alkaline activation treatment (KOH), c) bacterial treatment (BAC), d) ethyl silicate treatment (ES), e) nanosilica treatment (NS), and f) nanolime treatment (NL). The upper and lower images of each panel show the 2D and 3D view of the depth heatmaps (scale bar = 250 µm), respectively.

to a half plane of an elasto-plastic body at moderate speed ($V < 500$ m/s) according to Johnson [39]. Knowing the initial speed of the indenter tip (1.394 m/s) and the HLC value, we obtained the rebound velocity V' by:

$$V' = V\frac{HLC}{1000} \tag{5}$$

The ratio V'/V is known as the "coefficient of restitution", e, and according to Johnson [38]:

$$e^2 = \frac{V'^2}{V^2} = \frac{3\pi^{\frac{5}{4}}4^{\frac{3}{4}}}{10}\left(\frac{p_d}{E_{dr}}\right)\left(\frac{\frac{1}{2}mV^2}{p_dR^3}\right)^{-\frac{1}{4}} \tag{6}$$

Therefore, the reduced dynamic elastic modulus is:

$$E_{dr} = \frac{V^2}{V'^2}\frac{3\pi^{\frac{5}{4}}4^{\frac{3}{4}}p_d}{10}\left(\frac{\frac{1}{2}mV^2}{p_dR^3}\right)^{-\frac{1}{4}} \tag{7}$$

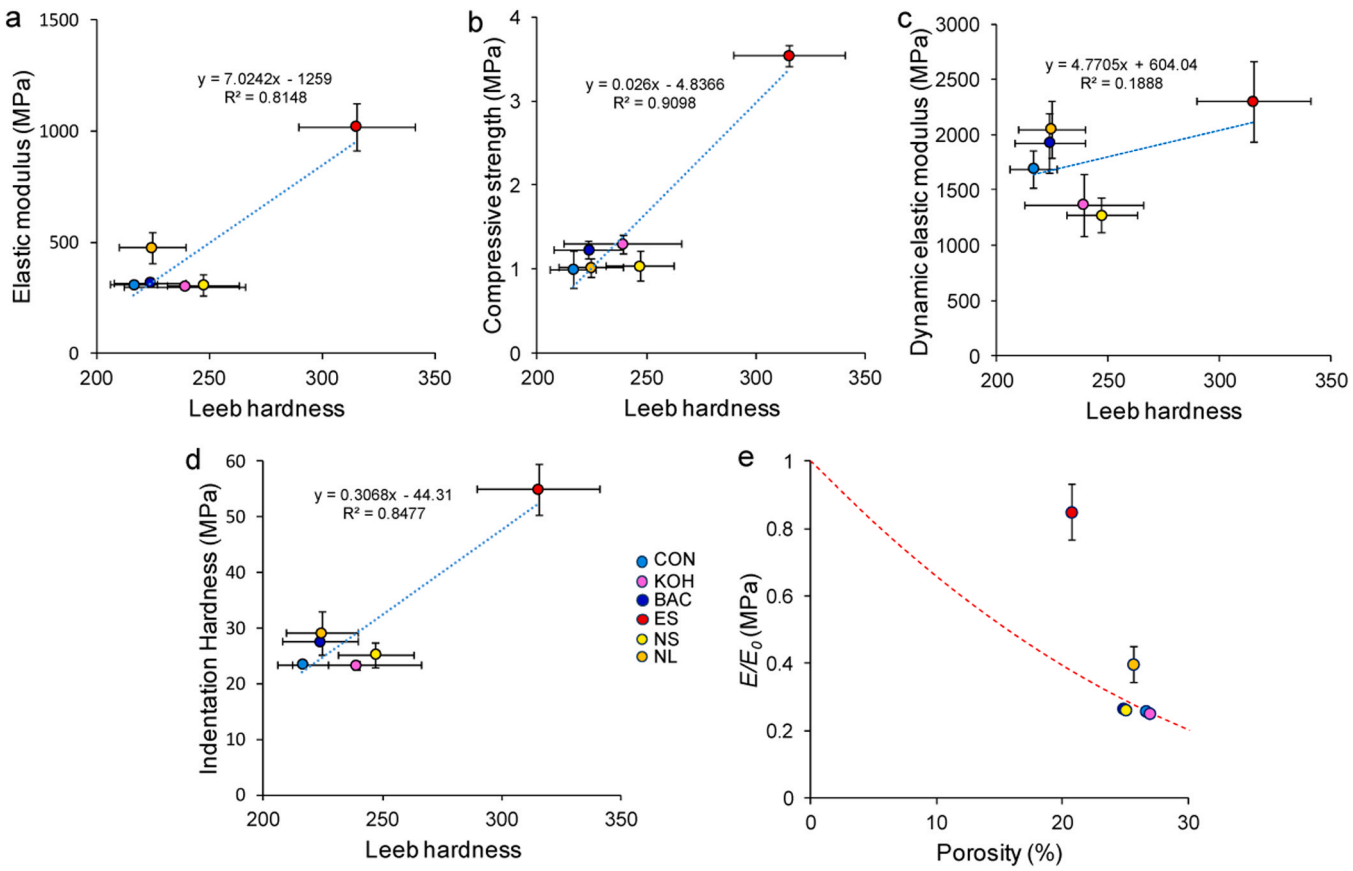

Fig. 8. Mechanical properties of untreated and treated earthen mock-ups. a) Elastic modulus determined using a contact model vs. Leeb hardness, b) unconfined compressive strength vs. Leeb hardness, c) dynamic elastic modulus determined using coefficient of restitution values vs. Leeb hardness, d) indentation hardness vs. Leeb hardness. The linear regression (dashed line) equations and R^2 values are included, and e) fitting of E/E_0 values vs. porosity of earthen mock-ups to an ellipsoidal pore model (red dashed line). Error bars show standard deviation.

where p_d is the mean contact pressure during dynamic loading, which is equal to

$$p_d = \frac{P}{\pi r^2} \tag{8}$$

where P is the applied load (immediately upon indenter rebound) and r is the radius of the projected area of the indentation mark. Note that Eq. (8) is equivalent to Eq. (4), used to calculate H. The values of p_d can also be used to calculate the yield strength Y, of the earthen mock-ups, because according to Tabor [73] $Y \approx 3p_d = 3H$.

Table 4 shows average values of HLC and dynamic elastic modulus E_d calculated using Eq. (7) and (3) for the different treatments tested here, as well as their corresponding yield strength (Y). In contrast to the modulus values calculated using the contact model which range between ~300 and ~1000 Mpa, values calculated using Eq. (7) and (3), which include the input of the coefficient of restitution determined by HLC, were about 2x times higher (from 1200 up to >2300 MPa). These latter values are not consistent with reported E values for earthen materials with comparable porosity and apparent density, which ultimately casts doubt on their reliability. In addition, there is no clear correlation between HLC and E_d values determined using this method (Fig. 8c), and average elastic index values of 0.017 ± 0.003 calculated using E_d values (i.e., H/E_d) were not consistent with reported values (see above). It is likely that the restitution coefficient determined by the Leeb rebound system is strongly affected by the plastic deformation undergone during impact; yielding values lower than expected for this type of material. As a result, the calculated E_d values are overestimated.

It should be noted that the yield strength values (marking the transition between elastic and plastic deformation under increasing load) for all the tested samples are relatively low (≤ 90 MPa), with the exception of the ES-treated mock-ups, which indicates that the materials are soft and clearly show elasto-plastic behavior. This is also consistent with the low values of UCS, similar to those reported for unstabilized rammed earth and adobe structures [45,69].

Considering that the rammed earth replicas were porous, we used different models to fit the variation of E determined using Eqs. (1) and (3), with fractional porosity, ø (determined by mercury intrusion porosimetry, Table 3). Tested models included the Voight, the Ramachrisna and Arunachalam, and the Pabst-Gregrovà models [74], as well as the models for overlapping spheres, ellipsoidal pores, overlapping spherical pores and overlapping ellipsoidal pores by Roberts and Garboczi [75]. The best fit was obtained using the model for ellipsoidal pores (Fig. 8e), considering a maximum E_0 value of 1200 MPa for highly compacted (with near zero porosity) rammed earth and assuming a value of 60 % porosity as percolation threshold when E drops to zero:

$$\frac{E}{E_0} = \left(1 - \frac{\phi}{0.6}\right)^{2.3} \tag{9}$$

We want to stress that the limited number of data points is a handicap for drawing a precise correlation between porosity and E/E_0 values; therefore, the results presented in Fig. 8e should be considered as trends but not as absolute values. Fig. 8e shows that E/E_0 values for both ES and NL plot above the model fitting curve for this type of material. This is consistent with the presence of significant amounts of cementing materials such as silica gel and calcium carbonate (calcite) with moduli higher than those of the substrate (~5–19 GPa and ~50–75 GPa, respectively) [71,72,76,77]. Conversely, the other treatments, including

NS, cluster close to the fitting curve, along with the value of the untreated control. The latter shows that a limited consolidation is achieved with these treatments. There is, however, an interesting outcome of the above analysis: it is remarkable that earthen mock-ups treated with NS display a relatively high HLC value, but at the same time, one of the lowest *E* values of all tested samples. This is paradoxical, as one would expect that high HLC values correspond to high *E* values. According to Kompatscher [34], however, a material with a lower modulus but yield strength similar to a material with a higher *E* value, would lead to a larger release of elastic energy upon impact of the Leeb indenter, resulting in higher restitution coefficient (*e*) and HLC values. This behavior is consistent with the formation of a ~60 μm thick silica gel layer on the earthen mock-up surface after NS treatment according to FESEM observations. The bulk mechanical behavior of the block is dominated by the earthen substrate that shows a marked plastic behavior, thus resulting in a low *E* value, whereas the surface behavior is dominated by the amorphous silica coating with a marked elastic-brittle behavior [76], resulting in a relatively high HLC. It is important to underline that this particular behavior would be detrimental to the overall mechanical behavior of the treated earthen material because the physical-mechanical discontinuity between the consolidant layer and the substrate creates a flaw where damage (cracks parallel to the substrate surface) starts/concentrates, while at the same time little or no effective bulk strengthening is achieved. Compatibility is also in question in the case of the ES treatment, showing a very large increase in *E*, as well as HLC and *H* values. Considering the superior penetration capacity of this consolidant, a relatively thick consolidated layer forms that is mechanically incompatible with the softer earthen substrate underneath. Previous research has shown this effect to be highly detrimental, as the hardened surface crust eventually detaches and falls off [78]. Finally, water-based treatments KOH and BAC have little effect on the mechanical properties assessed via HLC, even though the latter leads to an increase in the *E* and *H* values. This implies that the material gains strength, but its elastic response during the rebound testing does not improve if compared with the control. This means that the material behaves more plastically, thus becoming tougher, an effect that could be beneficial (i.e., to withstand stress associated with physical weathering). However, these changes are not drastic, and further research should evaluate whether the observed positive strengthening effects can be improved by modifying the treatment protocol.

3.6. Surface wettability and contact angle

The study of the surface wettability and water absorption kinetics reveals a very rapid and consistent response of the untreated substrate upon dosing of 4 μL water drops, which are fully absorbed after around 7 s (Fig. 9a). KOH does not influence the absorption behavior significantly, and the minor variations detected when compared with the untreated substrate are not statistically relevant, whereas BAC slightly delays the time required for the full absorption of the micro drops with an average value of 19 s. In all these cases, the very fast absorption does not allow for the stabilization of the micro drop shape in order to obtain reliable measurements of the initial contact angle after dosing. The remaining treatments, namely ES, NS and NL, induce a noticeable change in the surface water-related properties. An almost 5-fold increase in the average water absorption time is induced by ES and NS, although associated with much larger data dispersion compared to the control. This can be explained by the uneven surface accumulation of the consolidants and, particularly in the case of NS, by the presence of an extensively cracked silica gel layer as evidenced by microscopic observations. Such a layer can be responsible for increased absorption times as it can act as a physical barrier delaying the early-stage absorption. Additionally, the network of surface discontinuities caused by the cracks determines randomly distributed areas of preferential access for liquid water, contributing to a differential water absorption response at the micro-scale. This behavior is reflected in the initial contact angle results (Fig. 9b), showing a similar trend and data distribution for both treatments, with average values around 33° (ES) and 38° (NS). Considering the overall surface wettability properties, such contact angle values indicate that the initial hydrophilic behavior expected for this type of substrate is preserved after consolidation, and the wettability state can still be defined as strongly hydrophilic [79]. This is not surprising

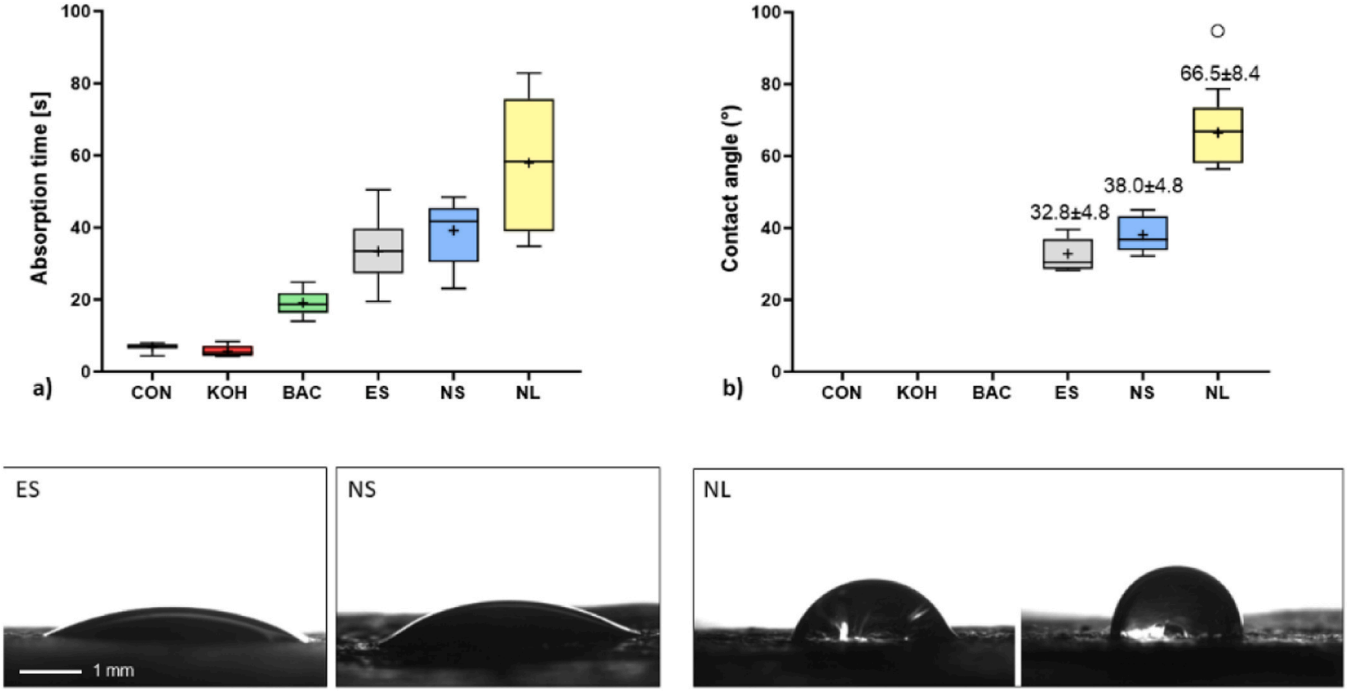

Fig. 9. Boxplots summarizing water microdroplets absorption kinetics (a) and initial contact angle values (b) of reference (CON) and treated earthen mock-ups (each box extends from 25th to 75th percentiles, whiskers indicate lower/higher absolute values, central line and cross indicate median and average values, respectively. Empty circles indicate outliers). Images at the bottom show representative drop shapes immediately after dosing.

considering that despite differences in the surface accumulation phenomena, particularly evident for NS, both treatments share similar chemical composition, although the final silica gel phases are formed following different curing routes. In contrast, the formation of a calcium carbonate-rich layer causes a significant change in the wettability properties after the NL treatment. We observed an almost 9-fold increase in the average absorption time compared to the untreated earthen mock-up and an increase in the initial contact angle values (>50°), rendering the surface weakly hydrophilic. The observed contact angles are consistent with those reported for calcite [80] and show similar tendencies as those previously reported for the same substrate obtained with conventional benchtop laboratory equipment [7]. While water absorption and contact angle data suggest improved water resistance of mock-ups treated with ES, NS, and NL, previous tests involving complete water immersion of earthen blocks revealed that only ES and, to a certain extent, KOH prolonged their durability under such extreme conditions [7]. This indicates that consolidation treatments only involving very thin surface layers render substrates slightly less hydrophilic but are not necessarily effective if direct water contact persists over longer periods of time.

4. Discussion

4.1. Consolidant performance

Our multi-analytical approach discloses significant differences in the film-forming propensity and in-depth distributions of consolidants, and their impact on key properties such as surface roughness and appearance, permeability, water behavior, and mechanical properties. Consolidation treatments based on alkaline activation (KOH) or bacterial biomineralization (BAC) only induced little changes in surface appearance and texture. The positive effect on mechanical strength and water resistance was very limited, and surface cohesion worsened. These results are in stark contrast to previous findings using more concentrated alkaline solutions (5 M KOH [12]) or applying biomineralization treatments to other substrates such as carbonate stone or gypsum [72,81]. This suggests that i) effective alkaline activation cannot be achieved with less concentrated (2 M) KOH solutions, and ii) the cementing capacity of activated indigenous carbonatogenic bacteria proved insufficient and warrants further research to optimize the treatment protocol and enhance effectiveness for extremely challenging earthen substrates (e.g., application of cultured ureolytic [82] or other carbonatogenic bacteria or choosing more favorable curing conditions [83]). Other alternative routes relying on enzyme induced carbonate precipitation [84], which have successfully been applied for soil cementation and dust control, might also have potential for the consolidation of earthen heritage structures.

Film-forming treatments based on nanoparticles (colloidal NS and NL dispersions) caused severe changes in surface appearance and a reduction in permeability, even though, they improved cohesion. Importantly, they only achieved very limited penetration, which is a major drawback according to previous studies [12]. In the case of the clay-rich substrate (especially with high content in expansive smectitic clays such as montmorillonite), clay swelling induced by the water-based NS consolidant likely further prevented adequate penetration. According to Norris [85] Na-montmorillonite may take up 10 g H_2O/g of clay and increase its volume by ~20 times. Immediately upon aqueous consolidant application, water enters the pores of the clay-rich substrate driven by capillary forces, leading to swelling and followed by additional expansion upon hydration of interlayer cations in the case of swelling clays [86]. Both phenomena will cause pore clogging and hinder the penetration of nanoparticles. In the case of the commercial product Nano Estel, a small amount of NaOH (<0.5 % according to the manufacturer) is added to stabilize the dispersion, which could theoretically counteract clay swelling to a certain degree by inducing flocculation [87]. However, such an effect was not observed here. Furthermore, penetration might even be hindered in soils with low clay content, where significant swelling is not expected. Depending on the pore size, these soils can act as filters and only allow the solvent (water) to penetrate deeper into the substrate, while nanoparticles are separated and accumulate at the surface [88]. In this respect, the high absorption capacity of clays due to their large specific surface area should also be considered [89].

In the case of the NL treatment, the opposing surface charge of (positively charged) lime particles and the (negatively charged) silicate grains in the substrate might have led to aggregation, causing clogging of near-surface pores and ultimately hindering further penetration [19]. In addition, Erdogan et al. [86] have shown that even though the swelling of expansive clays (bentonite) is 60 % lower in ethanol as compared to water (i.e., 680 % swelling in water versus 290 % swelling in ethanol), short-term swelling is much faster in ethanol, leading to a 4-fold increase in swelling after 5 minutes (i.e., 160 % swelling in ethanol versus 40 % swelling in water). Thus, pore clogging due to swelling cannot be ruled out in the case of alcoholic dispersions. Theoretically, other solvents could be selected to overcome this problem. According to Erdogan et al. [86] decanol provokes a slow response and very little clay swelling, while hexane causes no swelling at all. In addition, these long-chain alcohols with low vapor pressure could also reduce the risk of particle back-migration and (if adsorbed on the particle surface) prevent aggregation by promoting steric repulsion [90]. Based on these findings, film-forming treatments seem only suitable for substrates suffering from alteration limited to a very thin, millimeter-thick surface layer, which is normally not the case in earthen substrates. Future studies should, thus, focus on improving consolidant penetration by impeding nanoparticle aggregation and adverse consolidant-substrate interactions [24,90]. It should also be determined whether these consolidants demonstrate better efficacy in the case of deteriorated, extremely porous earthen substrates as compared to laboratory mock-ups.

Alkoxysilane (ES) was most effective in increasing mechanical strength and water resistance, while changes in surface appearance were generally acceptable except for a noticeable surface darkening. However, the significant increase in hardness and elastic modulus, together with a reduction in WVTR after ES treatment might lead to physico-mechanical incompatibility with the softer, more permeable earthen substrate underneath and ultimately accelerate degradation processes [91]. Additional research is required to determine whether highly diluted alkoxysilane solutions could overcome the described shortcomings and, at the same time, provide adequate cementation to guarantee long-term effectiveness. Alternatively, recently proposed consolidants based on alkoxysilane-nanoparticle (e.g., nanolime) mixtures could be tested on earthen substrates [92].

4.2. Evaluation of the multi-analytical approach

Using standard, lab-based analytical techniques the reliable performance and good accuracy of the proposed non-destructive or minimally invasive, portable methods were verified. The latter methods yield complementary and extremely valuable quantitative results for the evaluation of surface and sub-surface changes upon consolidation of earthen substrates. Importantly, all tested portable equipment is small, lightweight and battery-operated and can, thus, be used in remote sites without external power supply.

In this respect, it is also important to consider some limitations of conventional field-testing methods, such as Karsten tube or sponge tests, which can only inform on average (bulk) substrate properties (i.e., Karsten Tube testing involves a relatively large surface area (≥3 cm^2) and water amount, and measurements are influenced by the likely presence of large internal voids and cracks in the heterogeneous earthen substrates [93]). As such, these methods are thus not suitable to correctly describe subtle surface modifications and gauge the treatment effectiveness. To further complicate matters, the investigated sample

volume often varies or might even be unknown, depending on the substrate conditions (e.g., unknown depth of water absorption in the case of Karsten Tube testing [93]). The mobile surface analyzer tested here proved to be a valid alternative and allowed for measuring contact angle and small changes in absorption kinetics in most of the treated specimens under conditions that can be effectively replicated in different field applications (i.e., horizontal and vertical surfaces), thereby eliminating the need for destructive sampling. Due to the highly absorptive nature of the substrate it was impossible to measure the contact angle of some of the samples. This shortcoming is not specific to the portable equipment and has also been experienced with a conventional bench-top contact angle device.

The portable air permeameter successfully identified small changes in permeability induced by the consolidation treatments that were not detected by previous WVTR testing [7]. This method has the additional advantage to not alter the substrate permeability during testing (i.e., WVTR testing involves direct water contact and can induce changes in permeability due to hydration and swelling in the case of clay-rich earthen substrates). In addition, WVTR testing requires longer preparation and execution times and cannot be applied *in situ*. A recent study [30] found a good correlation between air permeability measurements and substrate porosity considering pore connectivity, implying that this non-destructive technique could be used *in situ* to assess water/-consolidant uptake by capillary absorption and evaluate weathering progress. However, the actual volume investigated via air permeability measurements also depends on substrate porosity/pore structure [31] and further tests are required to calibrate this technique, in particular in the case of earthen substrates that have not previously been tested with this method and often show significant variations in porosity and pore size distribution.

The *in situ* assessment of mechanical properties often involves ultrasonic pulse velocity measurements, which, however, might be challenging in the case of relatively soft, heterogeneous substrates with a very irregular surface [94]. Here, the applicability of Leeb surface hardness measurements has been demonstrated for earthen substrates. Its relatively low impact energy as compared to the widely used Schmidt hammer enables the detection of relatively small treatment-related surface mechanical changes of such soft building material and makes it almost non-destructive [95]. Furthermore, analysis of the indentation mark geometry upon hardness testing proved very useful in obtaining additional information on the mechanical properties of treated surfaces, in particular in the case of film-forming consolidants, without the need for any sampling. By using Hertz contact mechanics and dynamic contact mechanics, HLC testing can provide valuable quantitative information not only on indentation hardness but also on static and dynamic moduli. Note that ultrasound measurements can only yield the dynamic modulus, and its determination requires equipment capable of determining both Vp (speed of compression waves) and Vs (speed of shear waves), which is not standard in portable equipment [96]. However, only a small body of research exists on such soft building materials [97], and further studies involving a larger number of samples are necessary to validate our approach. Compositional and textural heterogeneity, including surface roughness, typical of this type of substrates, can have a significant impact on rebound hardness measurements, and a large number of measurements ($N \geq 70$) is recommended to improve data robustness [37,70].

Standard analytical techniques, applied in an advanced, less conventional manner proved very useful to complement results obtained with portable equipment in order to investigate consolidant distribution and corroborate treatment efficacy. FESEM elemental mapping of polished cross-sections proved extremely valuable, evidencing the very limited penetration of film-forming consolidants (NS and NL) and scarce cementation in the case of alkaline activation and biomineralization. However, elemental mapping was not able to provide unambiguous information regarding ES consolidant distribution, and indirect methods such as DR measurements are required to determine penetration [7]. It is also shown that VIS-light reflectance spectra can provide valuable additional information with respect to the commonly reported color parameters L^*, a^*, b^*, and ΔE^*, allowing for a better interpretation of the combined effect of color change and luminosity variations. Surface roughness analysis permitted a detailed surface characterization, and it proved particularly useful to consider several roughness parameters such as *Sa*, *Sz*, *Ssk*, and *Sku* to accurately describe surface changes induced by the consolidation treatment (i.e., material loss caused by water-based consolidants, consolidant accumulation phenomena and crack formation). Obtained data reveal good correlation with peeling test results, demonstrating that these two techniques are complementary and validating the usefulness of the peeling test for the *in situ* evaluation of surface cohesion. However, the number of studies involving peeling test application on earthen materials is still very limited [13,58] and more research is necessary to establish an appropriate protocol for such a heterogeneous substrate.

5. Conclusions

This comprehensive study highlights the effectiveness of integrating non-standard, portable methods with standard lab-based analytical techniques to assess surface and sub-surface changes following consolidation treatments. None of the consolidants showed optimal performance in the case of the earthen substrate, either due to limited penetration and formation of only a scarce amount of cementing phases, or by causing excessive physico-mechanical changes with implications for the overall compatibility. Penetration has been identified as a key parameter for successful consolidation treatments and further studies are imperative to enhance penetration of nanoparticle-based consolidants by reducing particle aggregation and consolidant-substrate interactions, improve treatment protocols and design optimized consolidants based on alkoxysilane-nanoparticle mixtures.

The suitability of a suite of portable equipments, including air permeameter, surface hardness tester, and mobile surface (contact angle) analyzer have been validated for their use on earthen substrates by this study. They provided accurate and reliable results, consistent with those obtained by standard lab-based analytical equipment as shown here, being a valuable addition to current on-site assessment capabilities and eliminating the need for destructive sampling. Importantly, the instruments were sufficiently sensitive to determine very subtle treatment-related changes limited to a thin surface layer. The advanced application of standard analytical techniques (FESEM elemental mapping using cross-sections) and detailed data analysis (application of contact mechanics theory for the evaluation of surface hardness measurements and a comprehensive analysis of roughness parameters) proved very useful to correctly determine consolidant distribution and changes in surface properties.

However, challenges due to substrate heterogeneity, even in the case of earthen mock-ups with controlled granulometry, have been encountered and additional research has to be performed to improve data robustness and validate these portable techniques for on-site use, preferably including a large number of earthen substrates with variable textural and compositional properties. The integrated approach outlined here will not only be instrumental for developing more efficient conservation treatments by correlating relevant substrate properties with consolidant performance, but could also be utilized for long-term, on-site monitoring of the weathering progression in built heritage materials, which is key to developing effective preventive conservation strategies. Finally, the comparative laboratory study using a substrate with controlled granulometry has proven indispensable to obtain a detailed understanding of the *modus operandi* of the different consolidants. Nevertheless, research focusing on the consolidation of earthen substrates has to be expanded and should include comparative *in situ* studies involving substrates with varying degrees of degradation in order to validate the laboratory results.

Funding

This research is part of the on-going collaboration agreements between the Getty Conservation Institute, the Patronato de la Alhambra y Generalife (Granada, Spain), and the Unidad Científica de Excelencia UCE-PP2016–05 of the University of Granada. This research was performed within the frame of the inter-institutional collaboration agreement "Patrimonio Cultural Árabe e Islámico (PACAI), UGR, Unidad Asociada al CSIC por la EEA-ILC (2024-2027)". This work was funded by Spanish Government grant PID2021.125305NB.I00 funded by MICIN/AEI/10.13039/501100011033 and by ERDF A way of making Europe, and research group RNM-179 (Junta de Andalucía), grant Microproyectos de Investigación (UCE2018–01, University of Granada). K. Elert is a contracted researcher funded by the Spanish Government (Ramón y Cajal contract, MICIN).

CRediT authorship contribution statement

Kerstin Elert: Writing – review & editing, Writing – original draft, Visualization, Resources, Project administration, Methodology, Investigation, Funding acquisition, Conceptualization. **Beril Biçer-Simşir:** Writing – review & editing, Investigation. **Davide Gulotta:** Writing – review & editing, Writing – original draft, Visualization, Resources, Methodology, Investigation. **Elena Correa:** Writing – review & editing, Investigation. **Carlos Rodriguez-Navarro:** Writing – review & editing, Writing – original draft, Methodology, Investigation.

Declaration of Competing Interest

The authors declare that they have no known competing financial interests or personal relationships that could have appeared to influence the work reported in this paper.

Data availability

Data will be made available on request.

Acknowledgements

We thank KBYO BIOLOGICAL S.L. (Spain) for supplying the patented nutritive solution M − 3 P. We also thank C. Cardell, F. Jroundi, M.T. González Muñoz, J.M. Azañón Hernández, and A. Leslie for their support and advice and the personnel of the Centro de Instrumentación Científica (CIC) of the University of Granada for help with FESEM analyses.

Appendix A. Supporting information

Supplementary data associated with this article can be found in the online version at doi:10.1016/j.conbuildmat.2024.137154.

References

[1] D. Camuffo, Physical weathering of stones, Sci. Total Environ. 167 (1995) 1–14.
[2] C. Rodriguez-Navarro, E. Doehne, Salt weathering: influence of evaporation rate, supersaturation and crystallization pattern, Earth Surf. Process. Landf. 24 (1999) 191–209.
[3] M. Steiger, A.E. Charola, K. Sterflinger, Weathering and deterioration, in: S. Siegesmund, R. Snethlage (Eds.), Stone in Architecture: Properties, Durability, Springer, New York, 2011, pp. 227–316.
[4] C. Moses, D. Robinson, J. Barlow, Methods for measuring rock surface weathering and erosion: A critical review, Earth Sci. Rev. 135 (2014) 141–161.
[5] K. Elert, C. Rodriguez-Navarro, Degradation and conservation of clay-containing stone: A review, Constr. Build. Mater. 330 (2022) 127226.
[6] G. Wheeler, Alkoxysilanes and the Consolidation of Stone, Getty Conservation Institute, Los Angeles, 2005.
[7] K. Elert, F. Jroundi, C. Benavides-Reyes, E.C. Gómez, D. Gulotta, C. Rodriguez-Navarro, Consolidation of clay-rich earthen building materials: A comparative study at the Alhambra fortress (Spain), J. Build. Eng. 50 (2022) 104081.
[8] E. Doehne, C.A. Price, Stone Conservation: An Overview of Current Research, The Getty Conservation Institute, Los Angeles, 2010.
[9] Conserving Stone Heritage: Traditional and Innovative Materials and Techniques, in: F. Gherardi, P.N. Maravelaki (Eds.), Cultural Heritage Science, Springer Nature Switzerland, Cham, 2022.
[10] S. Callegari, Rethinking Preservation at Fort Union National Monument, Master's Thesis, University of Pennsylvania, 2016.
[11] F.T. Madsen, M. Müller-Vonmoos, The swelling behaviour of clays, Appl. Clay Sci. 4 (1989) 143–156.
[12] K. Elert, P. Bel-Anzué, L. Monasterio-Guillot, E. Sebastián Pardo, Performance of alkaline activation for the consolidation of earthen architecture, J. Cult. Herit. 39 (2019) 93–102.
[13] V.E. García-Vera, A.J. Tenza-Abril, A.M. Solak, M. Lanzón, Calcium hydroxide nanoparticles coatings applied on cultural heritage materials: Their influence on physical characteristics of earthen plasters, Appl. Surf. Sci. 504 (2020) 144195.
[14] M. Lanzón, V. De Stefano, J.C.M. Gaitán, I.B. Cardiel, M.L. Gutiérrez-Carrillo, Characterisation of earthen walls in the Generalife (Alhambra): Microstructural and physical changes induced by deposition of $Ca(OH)_2$ nanoparticles in original and reconstructed samples, Constr. Build. Mat. 232 (2020) 117202.
[15] S. Rescic, M. Mattone, F. Fratini, L. Luvidi, Conservation of Earthen Bricks in Architecture: An Experimental Campaign to Test Different Treatments on Vernacular Built Heritage, Heritage 6 (2023) 1541–1566.
[16] Y. Praticò, F. Caruso, J. Delgado Rodrigues, F. Girardet, E. Sassoni, G.W. Scherer, V. Vergès-Belmin, N. Weiss, G. Wheeler, R.J. Flatt, Stone consolidation: a critical discussion of theoretical insights and field practice, Rilem Tech. Lett. 4 (2019) 145–153.
[17] K. Elert, E. Sebastián Pardo, C. Rodriguez-Navarro, Influence of organic matter on the reactivity of clay minerals in highly alkaline environments, Appl. Clay Sci. 111 (2015) 27–36.
[18] A. Ito, R. Wagai, Global distribution of clay-size minerals on land surface for biogeochemical and climatological studies, Sci. Data 4 (2017) 1–11.
[19] G. Torraca, G. Chiari, G. Gullini, Report on mud brick preservation, Mesopotamia 7 (1972) 259–286.
[20] M. Ambrosi, L. Dei, R. Giorgi, C. Neto, P. Baglioni, Colloidal particles of $Ca(OH)_2$: properties and applications to restoration of frescoes, Langmuir 17 (2001) 4251–4255.
[21] G. Ziegenbalg, M. Drdacky, C. Dietze, D. Schuch, Nanomaterials in Architecture and Art Conservation, Pan Stanford Publishing, Palo Alto, 2018.
[22] K. Elert, E.S. Pardo, C. Rodriguez-Navarro, Alkaline activation as an alternative method for the consolidation of earthen architecture, J. Cult. Herit. 16 (2015) 461–469.
[23] E. Franzoni, B. Pigino, C. Pistolesi, Ethyl silicate for surface protection of concrete: Performance in comparison with other inorganic surface treatments, Cem. Concr. Comp. 44 (2013) 69–76.
[24] R. Camerini, D. Chelazzi, R. Giorgi, P. Baglioni, Hybrid nano-composites for the consolidation of earthen masonry, J. Colloid Interface Sci. 539 (2019) 504–515.
[25] S. Ghadr, C.H. Liu, P. Mrudunayani, C. Hung, Effects of hydrophilic and hydrophobic nanosilica on the hydromechanical behaviors of mudstone soil, Constr. Build. Mat. 331 (2022) 127263.
[26] M.T. González-Muñoz, C. Rodriguez-Navarro, C. Jimenez-Lopez, M. Rodriguez-Gallego, Method and Product for Protecting and Reinforcing Construction and Ornamental Materials, Spanish Patent P200602030 (WO2008009771) 2008.
[27] CEN Technical Committee 346, EN 15886 - Conservation of cultural property - Test methods - Colour measurement of surfaces, 2010.
[28] G.P. Petropoulos, C.N. Pandazaras, J.P. Davim, Surface texture characterization and evaluation related to machining, in: J.P. Davim (Ed.), Surface Integrity in Machining, Springer, London, 2010.
[29] S. Brown, M. Smith, A transient-flow syringe air permeameter, Geophysics 78 (2013) D307–D313.
[30] W. De Boever, T. Bultreys, H. Derluyn, L. Van Hoorebeke, V. Cnudde, Comparison between traditional laboratory tests, permeability measurements and CT-based fluid flow modelling for cultural heritage applications, Sci. Total Environ. 554 (2016) 102–112.
[31] J.-D. Mertz, E. Colas, B. Yahmed, R. Lenormand, Assessment of a non-destructive and portable mini permeameter based on a pulse decay flow applied to historical surfaces of porous materials, in: J.J. Hughes, H. Torsten (Eds.), Science and Art: A Future for Stone. Proceedings of the 13th International Congress on Deterioration and Conservation of Stone, University of the West of Scotland, Paisley, 2016, pp. 415–422.
[32] O. Gilbert, L. Mol, O. Campbell, T. Blenkinsop, Permeability and surface hardness surveying of stone damaged by ballistic impact, Heritage 2 (2019) 1369–1389.
[33] D. Leeb, Dynamic hardness testing of metallic materials, NDT Int 12 (1979) 274–278.
[34] M. Kompatscher, Equotip-rebound hardness testing after D. Leeb. in: International Measurement Confederation, 9th Hardmeko - Hardness Measurements Theory and Application in Laboratories and Industries, Curran Associates, Inc., Red Hook, 2004, pp. 1–12.
[35] K.V. Gogolinskii, V.A. Syasko, A.S. Umanskii, A.A. Nikazov, T.I. Bobkova, Mechanical properties measurements with portable hardness testers: advantages, limitations, prospects, J. Phys. Conf. Ser. 1384 (2019) 012012.
[36] A.G. Corkum, Y. Asiri, H. El Naggar, D. Kinakin, The Leeb hardness test for rock: an updated methodology and UCS correlation, Rock. Mech. Rock. Eng. 51 (2018) 665–675.
[37] K. Wilhelm, H. Viles, Ó. Burke, Low impact surface hardness testing (Equotip) on porous surfaces – advances in methodology with implications for rock weathering and stone deterioration research, Earth Surf. Process. Landf. 41 (2016) 1027–1038.

[38] H. Aoki, Y. Matsukura, A new technique for non-destructive field measurement of rock surface strength: an application of the Equotip hardness tester to weathering studies, Earth Surf. Process. Landf. 32 (2007) 1759–1769.
[39] K.L. Johnson, Contact mechanics, Cambridge University Press, Cambridge, 1985.
[40] W.C. Oliver, G.M. Pharr, An improved technique for determining hardness and elastic modulus using load and displacement sensing indentation experiments, J. Mater. Res. 7 (1992) 1564–1583.
[41] H. Hertz, Über die Berührung fester elastischer Körper, J. für, die reine und Angew. Math. 92 (1882) 156–171.
[42] S.M. Walley, Historical origins of indentation hardness testing, Mat. Sci. Technol. 28 (2012) 1028–1044.
[43] Q.B. Bui, J.C. Morel, S. Hans, P. Walker, Effect of moisture content on the mechanical characteristics of rammed earth, Constr. Build. Mat. 54 (2014) 163–169.
[44] L. Miccoli, U. Müller, P. Fontana, Mechanical behaviour of earthen materials: A comparison between earth block masonry, rammed earth and cob, Constr. Build. Mat. 61 (2014) 327–339.
[45] F. Avila, E. Puertas, R. Gallego, Characterization of the mechanical and physical properties of unstabilized rammed earth: A review, Constr. Build. Mat. 270 (2021) 121435.
[46] S.K. Kang, J.Y. Kim, I. Kang, D. Kwon, Effective indenter radius and frame compliance in instrumented indentation testing using a spherical indenter, J. Mat. Res. 24 (2009) 2965–2973.
[47] M. Drdácký, J. Lesák, S. Rescic, Z. Slízková, P. Tiano, J. Valach, Standardization of peeling tests for assessing the cohesion and consolidation characteristics of historic stone surfaces, Mat. Struct. 45 (2012) 505–520.
[48] X.Q. Chen, B. Zhang, L. Xie, F. Wang, MWCNTs polyurethane sponges with enhanced super-hydrophobicity for selective oil–water separation, Surf. Eng. 36 (2020) 651–659.
[49] C. Bandl, N. Krempl, G. Berger-Weber, W. Kern, W. Friesenbichler, Application of organosilane coatings for improved anti-adhesive properties enabling facilitated demolding in polymer processing, J. Appl. Polym. Sci. 138 (2021) e50714.
[50] R.M. Barrer, Hydrothermal Chemistry of Zeolites, Academic Press, London, 1982.
[51] G.W. Scherer, Drying Gels, I. Gen. Theory, J. Non-Cryst. Sol. 87 (1986) 199–225.
[52] G. Borsoi, R. Veiga, A.S. Silva, Effect of nanostructured lime-based and silica-based products on the consolidation of historical renders, in: J.J. Hughes (Ed.), Proceedings of the 3rd Historic Mortars Conference, University of the West of Scotland, Glasgow, 2013, pp. 1–8.
[53] M.F. La Russa, S.A. Ruffolo, N. Rovella, C.M. Belfiore, P. Pogliani, C. Pelosi, et al., Cappadocian ignimbrite cave churches: stone degradation and conservation strategies, Period. di Mineral. 83 (2014) 187–206.
[54] C. Rodriguez-Navarro, K. Elert, R. Ševčík, Amorphous and crystalline calcium carbonate phases during carbonation of nanolimes: implications in heritage conservation, CrystEngComm 18 (2016) 6594–6607.
[55] M. Burgos-Ruiz, K. Elert, E. Ruiz-Agudo, H. Cölfen, C. Rodriguez-Navarro, Silica-Functionalized Nanolimes for the Conservation of Stone Heritage, Small (2023) 2300596.
[56] A. Michalopoulou, N.P. Maravelaki, N.A. Stefanis, P. Theoulakis, S. Andreou, V. Kilikogloul, I. Karatasios, Evaluation of nanolime dispersions for the protection of archaeological clay-based building materials, Mediterr. Archaeol. Archaeom. 20 (2020), 221-221.
[57] G. Borsoi, B. Lubelli, R. van Hees, R. Veiga, A.S. Silva, L. Colla, et al., Effect of solvent on nanolime transport within limestone: How to improve in-depth deposition, *Colloids Surf. A: Physicochem. Eng.* Asp. 497 (2016) 171–181.
[58] M. Lanzón, J.A. Madrid, A. Martínez-Arredondo, S. Mónaco, Use of diluted Ca (OH) 2 suspensions and their transformation into nanostructured $CaCO_3$ coatings: A case study in strengthening heritage materials (stucco, adobe and stone), Appl. Surf. Sci. 424 (2017) 20–27.
[59] A. Michalopoulou, E. Michailidi, E. Favvas, N.P. Maravelaki, V. Kilikoglou, I. Karatasios, Comparative evaluation of the morphological characteristics of nanolime dispersions for the consolidation of architectural monuments, Int. J. Archit. Herit. 14 (2020) 994–1007.
[60] W. Mokrzycki, M. Tatol, Color difference Delta E - A survey, Mach. Graph. Vis. 20 (2011) 383–411.
[61] O. García, K. Malaga, Definition of the procedure to determine the suitability and durability of an anti-graffiti product for application on cultural heritage porous materials, J. Cult. Herit. 13 (2012) 77–82.
[62] Y. Tamar, M. Tzabari, C. Haspel, Y. Sasson, Estimation of the porosity and refractive index of sol–gel silica films using high resolution electron microscopy, Sol. Energy Mater. Sol. Cells 130 (2014) 246–256.
[63] D. Strehlein, P. Schießl, Dark discoloration of fair-face concrete surfaces-transport and crystallization in hardening concrete, J. Adv. Concr. Technol. 6 (2008) 409–418.
[64] J. Das, B. Linke, Evaluation and systematic selection of significant multi-scale surface roughness parameters (SRPs) as process monitoring index, J. Mater. Process. Technol. 244 (2017) 157–165.
[65] N. Duboust, H. Ghadbeigi, C. Pinna, S. Ayvar-Soberanis, A. Collis, R. Scaife, K. Kerrigan, An optical method for measuring surface roughness of machined carbon fibre-reinforced plastic composites, J. Compos. Mater. 51 (2017) 289–302.
[66] M. Sedlaček, P. Gregorčič, B. Podgornik, Use of the roughness parameters S sk and S ku to control friction—A method for designing surface texturing, Tribol. Trans. 60 (2017) 260–266.
[67] F. Jroundi, M. Schiro, E. Ruiz-Agudo, K. Elert, I. Martín-Sánchez, M.T. González-Muñoz, C. Rodriguez-Navarro, Protection and consolidation of stone heritage by self-inoculation with indigenous carbonatogenic bacterial communities, Nat. Comm. 8 (2017) 279.
[68] M.M. Rafi, S. Khan, M.A. Bhutto, Experimental Assessment of Mechanical Properties of Adobe Masonry, J. Mater. Civ. Eng. 35 (2023) 04023319.
[69] A. Perić, I. Kraus, J. Kaluđer, L. Kraus, Experimental campaigns on mechanical properties and seismic performance of unstabilized rammed earth—a literature review, Buildings 11 (2021) 367.
[70] J. Desarnaud, K. Kiriyama, B. Bicer Simsir, K. Wilhelm, H. Viles, A laboratory study of Equotip surface hardness measurements on a range of sandstones: What influences the values and what do they mean? Earth Surf. Process. Landf.. 44 (2019) 1419–1429.
[71] C. Rodriguez-Navarro, L. Monasterio-Guillot, M. Burgos-Ruiz, E. Ruiz-Agudo, K. Elert, Unveiling the secret of ancient Maya masons: Biomimetic lime plasters with plant extracts, Sci. Adv. 9 (2023) eadf6138.
[72] D. Labonte, A.K. Lenz, M.L. Oyen, On the relationship between indentation hardness and modulus, and the damage resistance of biological materials, Acta Biomater. 57 (2017) 373–383.
[73] D. Tabor, The Hardness of Metal, Oxford University Press, Oxford, 1951.
[74] V. Presser, K. Gerlach, A. Vohrer, K.G. Nickel, W.F. Dreher, Determination of the elastic modulus of highly porous samples by nanoindentation: a case study on sea urchin spines, J. Mater. Sci. 45 (2010) 2408–2418.
[75] A.P. Roberts, E.J. Garboczi, Elastic properties of model porous ceramics, J. Am. Ceram. Soc. 83 (2000) 3041–3048.
[76] B.A. Latella, M.V. Swain, M. Ignat, Indentation and fracture of hybrid sol-gel silica films, in: J. Němeček (Ed.), Nanoindentation in Materials Science, IntechOpen, London, 2012, pp. 133–160.
[77] D. Mercier, A. Nicolay, A. Boudiba, X. Vanden Eynde, L. Libralesso, A. Daniel, M. Olivier, Mechanical properties and decohesion of sol–gel coatings on metallic and glass substrates, J. Sol. -Gel Sci. Technol. 93 (2020) 229–243.
[78] R. Aguzzi, A. Fiumara, A. Peroni, R. Ponci, V. Riganti, R. Rossetti, F. Soggetti, F. Veniale, L'arenaria della Basilica di S. Michele in Pavia: Ricerche sull'alterazione e sugli effetti dei trattementi conservativi, Atti Soc. Ital. di Sci. Nat. 114 (1973) 403–464.
[79] B. Pan, X. Yin, S. Iglauer, A review on clay wettability: From experimental investigations to molecular dynamics simulations, Adv. Colloid Interface Sci. 285 (2020) 1–24.
[80] C. Rodriguez-Navarro, E. Doehne, E. Sebastian, Influencing crystallization damage in porous materials through the use of surfactants: experimental results using sodium dodecyl sulfate and cetyldimethylbenzylammonium chloride, Langmuir 16 (2000) 947–954.
[81] F. Jroundi, M.T. Gonzalez-Muñoz, A. Garcia-Bueno, C. Rodriguez-Navarro, Consolidation of archaeological gypsum plaster by bacterial biomineralization of calcium carbonate, Acta Biomater. 10 (2014) 3844–3854.
[82] W. De Muynck, N. De Belie, W. Verstraete, Microbial carbonate precipitation in construction materials: a review, Ecol. Eng. 36 (2010) 118–136.
[83] X. Sun, L. Miao, T. Tong, C. Wang, Study of the effect of temperature on microbially induced carbonate precipitation, Acta Geotech. 14 (2019) 627–638.
[84] X. Sun, L. Miao, J. Yuan, H. Wang, L. Wu, Application of enzymatic calcification for dust control and rainfall erosion resistance improvement, Sci. Total Environ. 759 (2021) 143468.
[85] K. Norrish, The swelling of montmorillonite, Discuss. Faraday Soc. 18 (1954) 120–134.
[86] A.R. Erdogan, A.C. Whitford, T.R. Underwood, C. Sellick, R. Patel, N.T. Skipper, H. C. Greenwell, Swelling of compacted bentonite in organic solvents: Correlation of rate and extent of swelling with solvent properties, Appl. Clay Sci. 241 (2023) 107000.
[87] O. Karnland, S. Olsson, U. Nilsson, P. Sellin, Experimentally determined swelling pressures and geochemical interactions of compacted Wyoming bentonite with highly alkaline solutions, Phys. Chem. Earth 32 (2007) 275–286.
[88] A. Makó, M. Kocsis, G. Barna, G. Tóth, Mapping the storing and filtering capacity of European soils, Technical Report EUR28393 (2017) pp.54.
[89] R. Greene-Kelly, The specific surface areas of montmorillonites, Clay Min. Bull. 5 (1964) 392–400.
[90] E. Fratini, M.G. Page, R. Giorgi, H. Cölfen, P. Baglioni, B. Demé, T. Zemb, Competitive surface adsorption of solvent molecules and compactness of agglomeration in calcium hydroxide nanoparticles, Langmuir 23 (2007) 2330–2338.
[91] S. Siegesmund, R. Snethlage (Eds.), Stone in architecture: properties, durability, 5th Edition. Springer-Verlag, Berlin, 2014.
[92] A.M. Barberena-Fernández, M.T. Blanco-Varela, P.M. Carmona-Quiroga, Use of nanosilica-or nanolime-additioned TEOS to consolidate cementitious materials in heritage structures: Physical and mechanical properties of mortars, Cem. Concr. Comp. 95 (2019) 271–276.
[93] R. Hendrickx, Using the Karsten tube to estimate water transport parameters of porous building materials: The possibilities of analytical and numerical solutions, Mater. Struct. 46 (2013) 1309–1320.
[94] M. Shariati, N.H. Ramli-Sulong, M.M. Arabnejad, P. Shafigh, H. Sinaei, Assessing the strength of reinforced concrete structures through Ultrasonic Pulse Velocity and Schmidt Rebound Hammer tests, Sci. Res. Essays 6 (2011) 213–220.
[95] S.B. Çelik, İ. Çobanoğlu, Comparative investigation of Shore, Schmidt, and Leeb hardness tests in the characterization of rock materials, Environ. Earth Sci. 78 (2019) 1–16.
[96] V. Brotons, R. Tomás, S. Ivorra, A. Grediaga, J. Martínez-Martínez, D. Benavente, M. Gómez-Heras, Improved correlation between the static and dynamic elastic modulus of differe nt types of rocks, Mater. Struct. 49 (2016) 3021–3037.
[97] W. Hu, X. Liu, S. Fang, X. Chen, W. Gu, Q. Wei, Research on the building materials of adobe house in the Neolithic period at the Qingtai site, China, Archaeometry 64 (2022) 1411–1425.